Quantitative precipitation estimation from weather radars, personal weather stations and commercial microwave links

Overeem, Aart; Uijlenhoet, Remko; Leijnse, Hidde

DOI
10.1049/SBRA557H_ch2

Publication date
2024

Document Version
Final published version

Published in
Advances in Weather Radar. Volume 3

Citation (APA)
Overeem, A., Uijlenhoet, R., & Leijnse, H. (2024). Quantitative precipitation estimation from weather radars, personal weather stations and commercial microwave links. In V. N. Bringi, K. V. Mishra, & M. Thurai (Eds.), *Advances in Weather Radar. Volume 3: Emerging applications* (Vol. 3, pp. 27-68). Institution of Engineering and Technology. https://doi.org/10.1049/SBRA557H_ch2

Chapter 2

Quantitative precipitation estimation from weather radars, personal weather stations and commercial microwave links

Aart Overeem[1], Remko Uijlenhoet[2] and Hidde Leijnse[1]

2.1 Introduction

Precipitation information is employed for a myriad of purposes, such as climate monitoring and understanding the drivers behind extreme events, weather monitoring and nowcasting, natural hazard early warning (e.g. floods and landslides), crop production modelling and rainfall index crop insurance, extreme value modelling and (sewerage) design purposes, evaluation of extreme events and their impact, and validation of weather prediction and climate model output (Chapters 1 and 3 of this book). Hence, localised, timely, regularly updated and accurate precipitation information is highly relevant.

The focus of this chapter is on quantitative precipitation estimation (QPE) by ground-based sensors of liquid precipitation (rain) at the Earth's surface, which is the dominant precipitation type in the mid-latitudes and (sub)tropics. Traditionally, precipitation is observed in situ by rain gauges or retrieved via remote sensing by ground-based weather radars or satellites. Government rain gauge networks (often nationally operated by national meteorological and hydrological services (NMHSs)) can provide accurate local rainfall estimates, but their densities are often too low to capture the spatial rainfall variability. Their estimates are commonly combined with those from weather radars, which do provide wide coverage but are prone to many sources of error. Figure 2.1 provides worldwide maps with estimated coverage by radars and rain gauges and two so-called opportunistic sensors. The estimated 1308 weather radars provide coverage over large parts of the Americas, China, Europe, India, Japan, Oceania, South Africa and South East Asia (Figure 2.1(a)). Coverage over Africa and large parts of Asia is poor or even non-existent. The coverage by rain gauges from NMHSs and other institutes, as obtained from the Global Telecommunication System (GTS), reveals

[1]R&D Observations and Data Technology, Royal Netherlands Meteorological Institute, De Bilt, The Netherlands
[2]Department of Water Management, Faculty of Civil Engineering and Geosciences, Delft University of Technology, Delft, The Netherlands

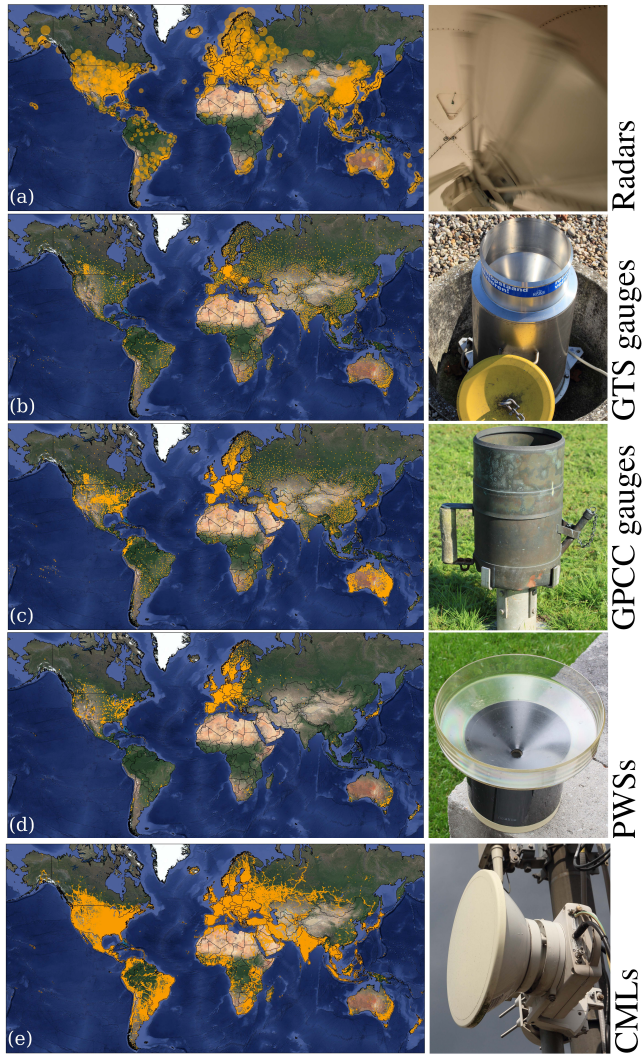

Figure 2.1 Worldwide coverage of ground-based weather radars (a), GTS rain gauges (b), GPCC rain gauges from the Full Data Monthly Product (c), Netatmo personal weather stations (PWSs) (d) and cell phone towers as proxy for commercial microwave links (CMLs) (e). Details on the construction of the maps are provided in Box 2.1. Map data © 2023 Google.

poor coverage compared to radar (Figure 2.1(b)). They constitute an important part of the (near) real-time rain gauges from government institutes. The coverage of rain gauges used in a non-real-time Global Precipitation Climatology Centre (GPCC) product is much higher [1,2] (Figure 2.1(c)).

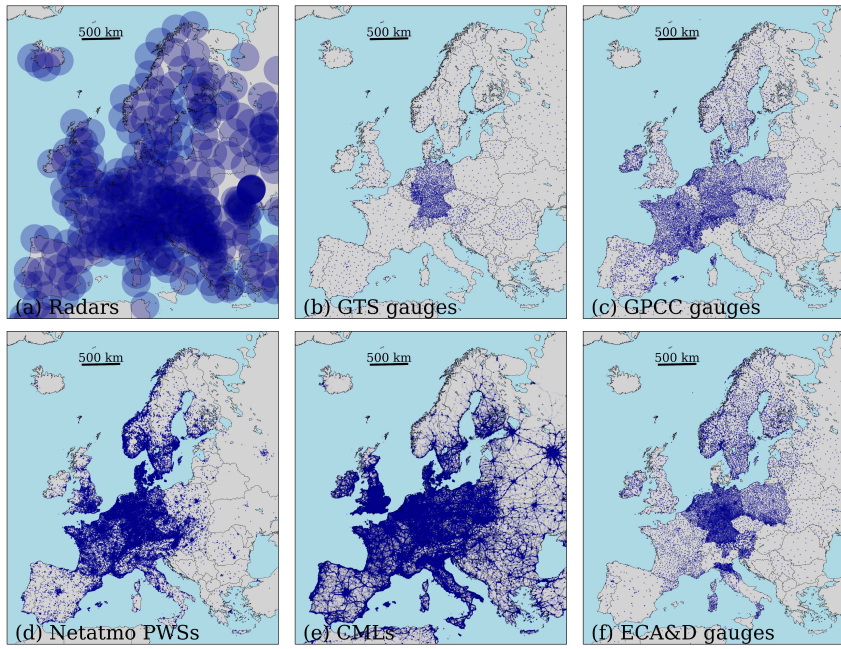

Figure 2.2 European coverage of ground-based weather radars (a), GTS rain gauges (b), GPCC rain gauges from the Full Data Monthly Product (c), Netatmo personal weather stations (PWSs) (d), cell phone towers as proxy for commercial microwave links (CMLs) (e) and rain gauges from the European Climate Assessment and Dataset project [8,9] (ECAD; https://www.ecad.eu). These provide daily timeseries. Locations were obtained mid-June 2022 over the period 1 September 2019 through 31 August 2020 (f). Details on the construction of the maps are provided in Box 2.1. Maps made with Natural Earth. Free vector and raster map data © https://naturalearthdata.com.

Box 2.1: Construction of global coverage maps

The derivation of worldwide coverage maps is not straightforward. Here, the underlying databases of locations and the chosen settings are discussed. The physical footprint for radars is large and plotted in Figure 2.3. In contrast, the physical footprints for rain gauges and commercial microwave links (CMLs) are much smaller, but due to spatial rainfall correlation, their effective coverage is larger. For rain gauges and CMLs, the plotted coverage on a world map is much larger than the physical footprint or even effective coverage to enhance visibility.

Radars

Most radar locations were obtained in February 2023 from a World Meteorological Organization (WMO) database (https://wrd.mgm.gov.tr/Home/Wrd). Radars (RAdio Detection And Ranging) were assumed to have a 200-km range, independent of the used radio frequency band. Note that the large majority of radars operate at C- or S-band and will at least meet this range. Research radars were not considered. Apart from the operational ones, also the partly operational (6), planned (16) and pre-operational (4) ones were selected. In total 1037 radar locations were obtained in this manner. On top of this the following radar locations have been added:

- Belgium (one radar): location of radar operated by Flanders Environment Agency obtained from a radar file from July 2021. Radar is currently operational (June 2023).
- China (197 radars): obtained from https://www.rainviewer.com/radars/china.html in May 2023. A clear resemblance is found with the locations presented in Minda and Nakamura [3], who report 217 radars.
- India (nine radars): found by employing https://mausam.imd.gov.in/ in June 2023 (sometimes coordinates are stated in maps), and only selecting those that provide recent radar images for that location. For six out of nine locations, the presence of a radar was confirmed by a Google Maps satellite image (and for three out of these six locations confirmed by the exact location as given in radar images). The other three locations were found by consulting the contents of the downloaded web page, which usually seems to provide approximate locations. Note that for two radar locations, the coordinates from the WMO radar database were replaced by coordinates obtained from a Google Maps satellite image, because one radar was located in the Bay of Bengal and one radar had the same coordinates as another radar.
- Latvia (one radar): live radar image shown at https://videscentrs.lvgmc.lv/karte/meteorologiska-radara-informacija in May 2023. Found in the WMO database (status non-reporting). Exact location cannot be found by using Google Maps.
- Lithuania (two radars): live radar image shown at http://www.meteo.lt/en/radar-information. Locations obtained from https://www.rainviewer.com/radars/lithuania.html in May 2023 and confirmed by a visible radar radome on a Google Maps satellite image.
- Mongolia (one radar): live radar image shown at http://tsag-agaar.gov.mn/ in May 2023. Exact location cannot be found by using Google Maps. Location taken from https://www.rainviewer.com/radars/mongolia.html.
- Morocco (seven radars): found in the WMO database as stand-by radars, but operational according to https://www.marocmeteo.ma/fr/observation.

- Myanmar (two radars): found by employing https://www.moezala.gov.mm/radar-image-1 in February 2023 and confirmed by a visible radar radome on a Google Maps satellite image.
- Nepal (one radar). Old radar image shown at https://www.dhm.gov.np/mfd/radar in June 2023. Approximate radar location provided by Talchabhadel *et al.* [4]. Exact location found by using Google Maps satellite image. Radar is currently out of service and needs to be repaired or replaced.
- New Caledonia (three radars and one additional radar, but this one is currently not available and has not been taken into account): live radar image shown at https://www.meteo.nc/nouvelle-caledonie/observations/images-radars in May 2023. Exact location cannot be found by using Google Maps. Locations taken from https://www.rainviewer.com/radars/new-caledonia.html. Locations could not be confirmed by Google Maps.
- Nigeria (four radars): obtained from https://www.google.com/maps/d/viewer?mid=1GIb9XpFV1dXq-ISwDeI9hYIJ0mu4QwNc&ll=9.139781073721903\%2C7.63924831988442&z=7 in February 2023.
- Porto Santo Island (one radar; Portuguese archipelago of Madeira): approximate location obtained from https://www.ipma.pt/en/otempo/obs.radar/index.jsp in May 2023, which shows live radar images. Exact location found by using Google Maps satellite image, which reveals a visible radar radome.
- Réunion Island (one radar; France overseas department): approximate location obtained from https://meteofrance.re/fr/images-radar in May 2023, which shows live radar images. Exact location found by using Google Maps satellite image, which reveals a visible radar radome.
- Republic of Fiji (three radars): approximate locations obtained by combining https://www.met.gov.fj/index.php?page=radar (Fiji Meteorological Service), which shows live radar images (May 2023), and Google Maps.
- Saudi Arabia (11 radars): found by employing https://www.rainviewer.com/radars/saudi-arabia.html in May 2023, and only selecting those that agree with the rough locations shown on official radar reflectivity composites on the website of the National Center for Meteorology (NCM) of Saudi Arabia (https://ncm.gov.sa/Ar/Weather/RegionWeather/Pages/KSA-IRIS.aspx; not accessible outside Saudi Arabia). For 10 out of 11 locations, the presence of a radar was confirmed by a Google Maps satellite image. Note that for the only radar location which was already obtained from the WMO radar database, the coordinates were replaced by coordinates obtained from a Google Maps satellite image.
- The Philippines (20 radars): data source (February 2023): Climate and Agrometeorological Data Section (CADS), Philippine Atmospheric, Geophysical and Astronomical Services Administration (PAGASA).

- Vietnam (six radars): found by employing https://www.rainviewer.com/radars/vietnam.html in February 2023 and only selecting those confirmed by a visible radar radome on a Google Maps satellite image.

Some radars may not be operational or temporarily out of service due to maintenance; other radar locations may still be missed. Likely, the radar coverage is underestimated.

GTS gauges

Because of incomplete coverage, gauge locations were not obtained from the official WMO OSCAR database (https://oscar.wmo.int/surface/#/search/station). The locations of 11,076 rain gauges contributing to the GTS, as used in the near real-time operational GPCC Monitoring Product [2], were obtained from January 2023. These represent an important part of the automatic rain gauges from government agencies providing (near) real-time data.

GPCC gauges

The locations of 32,036 rain gauges were obtained as used in the GPCC Full Data Monthly Product from January 2012 (V.2022) [2]. The large majority of stations are expected to be still operational in 2023, but due to latency of rain gauge data becoming available, the locations from 2012 were taken. Most stations typically provide daily accumulations once a day.

PWSs

The Netatmo rain gauge locations were downloaded in February 2023 using the Netatmo API (https://dev.netatmo.com/apidocumentation/weather). World wide, the number of automatic rain gauges at personal weather stations (PWSs) from all brands is expected to be at least a few hundred thousand.

CMLs

The cell phone tower locations were obtained from the OpenCelliD Project (https://opencellid.org/) after registration, which is licenced under a Creative Commons Attribution-ShareAlike 4.0 International License (https://creativecommons.org/licenses/by-sa/4.0/). OpenCelliD estimates cell phone tower locations by averaging locations of smartphones that receive radio signals from a specific cell phone tower. The smartphone locations are retrieved from a small number of apps. The following selections were performed, resulting in ∼34 million cell phone tower locations:

- Locations for which the approximate area within which the cell could be is smaller than 10 km.
- Locations that have been estimated from at least two samples.
- Locations that were last recorded after 1 January 2015.

So-called macro and small cell backhaul links between cell phone towers are estimated at 9.7 million in 2021. They consist of copper cables (2%), satellite links (2%), glass fibre-optic cables (31%) and CMLs (65%). The estimated 4.6 million CMLs (47%) operating in the 6–56 GHz range are the most useful

for rainfall estimation. Their number is expected to increase to 6 million in 2027, although their relative share will decrease (35%), mainly due to an increase in glass fibre-optic cables (42%) and partly due to higher frequency CMLs [5]. The large CML backhaul share underpins that cell phone tower locations can serve as a proxy for CML locations. Nevertheless, note that in some regions, the actual coverage of the backhaul CML network will be much lower due to the use of glass fibre-optic cables.

High rain gauge coverage by government agencies is found in Europe and parts of North America and Oceania, and low(er) coverage in South America, Africa and parts of Asia, consistent with [6,7]. The total number of rain gauges from operational meteorological networks is estimated to be at most 0.25 million (often daily manual rain gauges), while the number of those giving useful near real-time observations is estimated to be 8,000–12,000 [7]. The coverage by radars and rain gauges is insufficient for large parts of the Earth's land surface.

Satellites provide the widest coverage and are the only means of precipitation information over vast areas of the Earth's land surface and oceans. The added value of satellite QPE will be limited for areas with good radar and rain gauge coverage. Precipitation is retrieved indirectly via visible and infrared channels from geostationary satellites at typically ∼3 km resolution every 15 min, or more directly via radiometers on a constellation of low orbiting satellites. They provide higher accuracy but, in contrast to geostationary satellites with their continuous coverage, have longer revisit times of approximately a few hours for a constellation of satellites (but 24 h or longer for an individual satellite) and lower spatial resolution. Higher accuracy can be achieved by the space-borne precipitation radar aboard the Global Precipitation Measurement (GPM) mission's core satellite (Chapter 5 of Volume 1; the CloudSat satellite cloud radar and CubeSat satellites being the only other existing space-borne precipitation radars). It has a ∼5 km spatial resolution, but its revisit time is only ∼1 day for a given location.

Hence, across large parts of the Earth's continents, there is a need for supplementary precipitation information. This can be obtained from opportunistic sensors, often not even designed for precipitation retrieval. The two most mature techniques for opportunistic sensing of precipitation are personal weather stations (PWSs) and commercial microwave links (CMLs). The PWS or third-party rain gauges are Internet of Things (IoT) devices, which are typically purchased and operated by weather enthusiasts. Figure 2.1(d) shows that the coverage of one brand of these crowdsourced rain gauges, from private company Netatmo, is mainly limited to Europe, the United States of America, Japan, and parts of Australia and Canada. There, the network densities are generally much higher than those from government rain gauges. This is illustrated for Europe in Figure 2.2(b)–(d) and (f), where also locations from the government rain gauges from the European Climate Assessment and Dataset project (ECAD) [8,9] (https://www.ecad.eu) are visualised. Because differences in network densities in world maps are difficult to

discern due to the size of the plotted points, these zoomed in maps for Europe are given for all sensors (Figure 2.2). An overview of (sub-daily) rain gauge datasets for Europe is provided by Van der Schrier *et al.* [10]. PWSs are usually found in areas with radar coverage and often lack a heating device, limiting their applicability to liquid precipitation (rainfall) estimation.

CMLs are radio connections used globally in cellular telecommunication networks. The rain-induced signal attenuation between the transmitting antenna at one base station (or cell phone tower) and the receiving antenna at another base station can be computed and converted to averaged rainfall intensity over a path of typically a few hundred metres up to a few tens of kilometres. Figure 2.1(e) shows the locations of cell phone towers, which are used here as a proxy for CML locations. Worldwide $\sim$5 million CMLs are used in telecommunication networks [11]. Their largest potential for rainfall estimation lies in areas which are mostly not covered by the other ground-based sensors, typically low- and middle-income countries (LMICs) in (sub)tropical regions, but for which the required cellular communication infrastructure is already in place. This is especially the case for Africa and for parts of Asia and South America (Figure 2.1(e)).

For QPE, not only knowledge of the sensors is important, but also knowledge of the observed hydrometeors. This concerns both physical and statistical aspects (coverage and correlation in time and space). Rainfall consists of a collection of drops with various sizes, shapes and fall speeds and can be described by a so-called drop size distribution (Chapter 6 of Volume 2), the shape of which is determined by coalescence and break-up (and potentially evaporation) of drops [12]. Precipitation types, their size distribution and fall velocities can be observed with disdrometers, making them important sensors to derive parameter values for precipitation retrieval relationships (Chapter 6 of Volume 2). Disdrometers are not addressed in this chapter because of their much lower density compared to government rain gauges. The ability to approximate the actual rainfall accumulation at the Earth's surface is determined by many factors and varies from sensor to sensor, each having its own sampling volume or spatial support. Radars provide 3D volumetric data, whereas CMLs provide path-averaged (line segment) data and PWSs provide point observations. Typically, these sensor data are interpolated to 2D gridded rainfall fields. Figure 2.3 illustrates the sensors' footprints, the typical conversions and the interpolation. QPE is indirect for remote sensing devices, because it depends on the conversion from remote observables aloft to rain rates at the ground. It is governed by the interplay of electromagnetic radiation and hydrometeors: received signal power (radar reflectivity factor Z) or specific differential phase (K_{dp}; Chapter 5 of Volume 2) for radars, and specific attenuation (k) for CMLs. For rain gauges, QPE is direct by receiving the precipitation falling at the Earth's surface. Still, environmental conditions (notably wind effects), device set-up and sensor accuracy can lead to deviations with respect to the actual rainfall.

Table 2.1 provides a summary of the characteristics of QPE with radars, rain gauges, PWSs, CMLs and satellites. Other overviews are provided by Barthès and Mallet [13] and Priebe [14]. The quality of radar QPE depends on the applied processing, but adjustment with rain gauge data remains usually desirable.

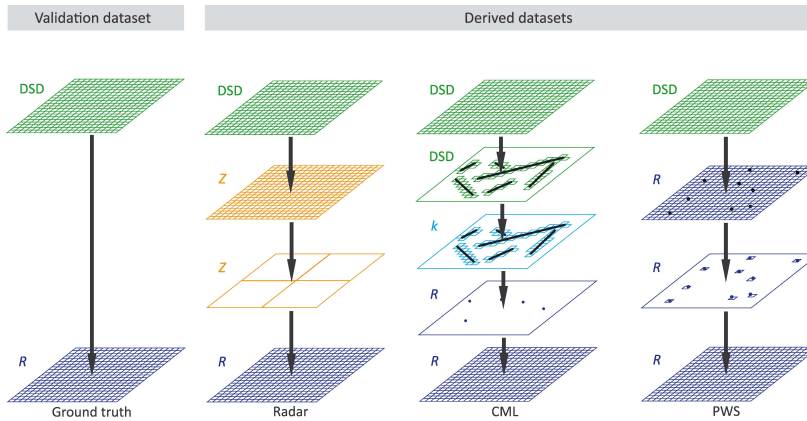

Figure 2.3 From drop size distributions (DSDs) to derived rainfall fields for radars, CMLs and PWSs. Figure taken from [15].

Table 2.1 Overview of sensors for rainfall estimation at the Earth's surface and their typical temporal and spatial resolutions, coverage and cost (related to installation and maintenance, not to quality control, rainfall retrieval and product dissemination).

Sensor	Temporal resolution	Sampling area	Coverage	Cost
Radars (X-band)[a]	Seconds to 1 min	A few tens of m×1°	2,000–30,000 km^2	Medium
Radars (C- and S-band)[a]	5–15 min	0.4 km×1°/1–2 km	30,000–650,000 km^2	High
Government rain gauges	1 min to 24 h	A few dm^2	Local	Medium
PWS rain gauges	5 min	A few dm^2	Local	Low
CMLs[b]	10 s to 15 min	0.1–20 km	Local–regional	Low
Geostationary satellites	5–15 min	1 – a few tens of km^2	World	Very high
Constellation of satellite radiometers[c]	A few hours	A few tens–hundreds of km^2	Snapshot	Very high
Space-borne radars[c]	24 h to days	5 km	Snapshot	Very high

[a]Their effective spatial resolution may be lower, coverage depends on the used wavelength (X-, C- or S-band), and the coverage for which accurate QPE is obtained may be much lower. Costs per km^2 are not that high.

[b]Provide rainfall estimates over a narrow path. Costs are low because the infrastructure is already in place.

[c]Only provide a snapshot during their overpass, typically from 60°S to 60°N.

Government rain gauges provide accurate, but only local, estimates if well maintained. PWSs and CMLs can give reasonable rainfall estimates after careful quality control (QC) or rainfall retrieval, respectively. Satellite QPE has usually poor accuracy, but higher accuracy for space-borne radars.

In this chapter, the quality of QPE with radar data, PWS data and CML data is evaluated for the Netherlands, a mid-latitude country with a temperate climate. This will provide insight into the stand-alone performance of opportunistic sensors, where the Netherlands acts as a test bed with relatively accurate reference data. First, the employed datasets are described. Next, three consecutive sections discuss QPE with radars, PWSs and CMLs. Apart from the evaluation in each section, details are provided on each sensor (Boxes 2.2–2.4). For radars, an overview and illustration of sources of error in QPE and of algorithms to improve QPE are provided. For PWSs, factors affecting the quality of rainfall estimates and QC algorithms to remedy these are discussed. For CMLs, the principle of rainfall retrieval and the encountered sources of error are described. Finally, a summary and outlook are provided, focusing on (1) improving radar QPE by merging with CML or PWS rainfall estimates and (2) showcasing the potential of CMLs for rainfall estimation in LMICs.

2.2 Datasets and evaluation metrics

Figure 2.4 provides an overview of the locations of the employed radars and government rain gauges from the Royal Netherlands Meteorological Institute (KNMI), PWS gauges from brand Netatmo and CML paths of mobile network operator (MNO) T-Mobile NL. The number of PWS and CML locations, which can potentially provide (near) real-time data, is much higher than the number of KNMI rain gauges. The contrast is even larger when only considering KNMI rain gauges at automatic weather stations (AWSs), which can provide near real-time information. The daily accumulations from KNMI's manual rain gauge network ($\sim$1 gauge/100 km^2) are used for evaluation of (merged) radar accumulations and interpolated PWS and CML rainfall maps. Validated and complete AWS and manual KNMI rain gauge records are used (also for the merged radar datasets), which are not available in real-time. The PWS data span the period June–August 2020; the open CML data [16] span the period June–August 2012. These periods are different because no coincident CML and PWS data could be obtained covering the entire Netherlands over the same 3-month period simultaneously.

A gauge-adjusted radar precipitation dataset is used to evaluate daily PWS point and CML path-averaged accumulations, interpolated PWS and CML rainfall maps and merged radar datasets. It is also employed to derive a 25-year mean annual precipitation climatology from 1998 to 2022. This climatological radar dataset, with $\sim$0.9 km^2 spatial resolution ($\sim$6 km^2 for the 25-year climatology), combines a daily spatial adjustment using the manual rain gauge accumulations with an hourly mean-field bias adjustment employing the AWS accumulations [17,18]. It is denoted in this chapter as 'radars + gauges'. Also a radar dataset

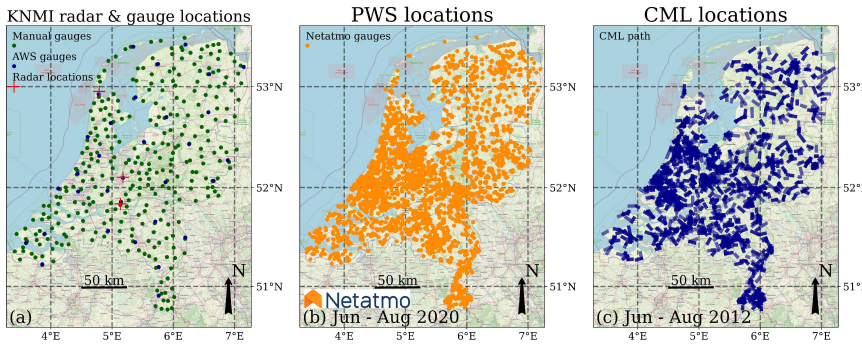

Figure 2.4 Map of the Netherlands with locations of 3 KNMI radars, 32 automatic and 320 manual KNMI rain gauges. The number and location of gauge locations are from 30 June 2020 and can slightly vary within and between the three periods in this study. The number of Netatmo personal weather stations (June–August 2020; after applying quality control and accumulation to 1-h rainfall as described in Section 2.4.1) is more than 100 times larger than the number of KNMI automatic rain gauges. For commercial microwave links, data from over 1,500 paths are available (June–August 2012; part of the former network of one of the three MNOs in the Netherlands). Paths are shown for which at least one 15-min rainfall estimate was obtained. Note that data from two radars were used, and that the radar in the middle was replaced by the southernmost radar in January 2017. Map data ©OpenStreetMap contributors 2023. Distributed under the Open Data Commons Open Database License (ODbL) v1.0.

without this gauge adjustment is evaluated ('radars') or merged with either AWS, PWS or CML accumulations. Finally, four different (un)adjusted radar datasets are evaluated for the period August 2017 to July 2018 (see Section 2.3.7). Table 2.2 provides an overview of the employed rainfall datasets that are evaluated or used as reference.

Several metrics are used to evaluate the performance of the various daily precipitation datasets in scatter density plots. Residuals are computed as the precipitation accumulation from the evaluated dataset minus the reference precipitation accumulation. The relative bias is computed as the average of the residuals divided by the average of the reference, expressed as a percentage. The standard deviation of the residuals is divided by the average precipitation accumulation from the reference to obtain the value for the coefficient of variation (CV). Finally, the squared Pearson correlation coefficient (ρ^2), or coefficient of determination (i.e. the fraction of the variance in the reference that is explained by a linear regression model), is computed between the evaluated dataset and the reference.

Table 2.2 Overview of the different rainfall datasets that are evaluated or used as reference datasets.

Dataset title in figures	Description
Radars	Daily gridded radar dataset
Interpolated manual gauges	Daily gridded manual rain gauge dataset (reference)
Manual gauges	Daily point accumulations (reference)
Radars + gauges	Daily gridded climatological dataset (reference)
PWSs	Daily interpolated maps at the radar grid
PWSs, interpolated values	Daily interpolated values at manual rain gauge locations
PWSs, point values	Daily *in situ* values[a]
CMLs	Daily interpolated maps at the radar grid
CMLs, interpolated values	Daily interpolated values at manual rain gauge locations
CMLs, path-averaged values	Daily path-averaged values[b]
Radars + AWSs	Daily gridded dataset from merged 1-h radar and AWS data
Radars + PWSs	Daily gridded dataset from merged 1-h radar and PWS data
Radars + CMLs	Daily gridded dataset from merged 1-h radar and CML data

[a]Are compared to grid cell values from 'radar + gauges' dataset.
[b]Are compared to path-averaged values from 'radars + gauges' dataset.

2.3 QPE with ground-based weather radars

2.3.1 Signal processing

The chain for QPE with ground-based weather radars starts with signal processing at the radar site. Generally, Doppler filtering is applied to remove the part of the power caused by stationary non-meteorological echoes (Chapter 2 of Volume 1). Horizontally polarised echo powers are converted to radar reflectivity factors by means of the radar equation [25]. In case of dual-polarisation (dual-pol) or polarimetric radars (Chapter 2 of Volume 1), this is also done for vertically polarised echo powers. In addition, dual-pol radars provide phase measurements. Monitoring and calibration in the signal processor are important to detect and correct for hardware-related errors, such as antenna pointing offsets, which can seriously affect the quality of QPE (Chapter 2 of Volume 2, [26]).

Box 2.2: Introduction to weather radars

Pulsed ground-based weather radars are employed by NMHSs to obtain QPE with large coverage at a spatial resolution of a few km every 5–15 min (Chapters 1 and 2 of Volume 1). This is achieved by a long processing chain, typically spanning from signal processing, application of correction algorithms to 3D radar data, conversion to 2D precipitation fields and adjustment with rain gauge accumulations. These steps are needed not only to convert received signal amplitudes and phases to QPE (Chapter 5 of Volume 2) but also to correct sources of error in radar QPE, many of them indicated in

Figure 2.5. Extensive overviews of sources of error in radar QPE and algorithms to address these are provided by Joss and Waldvogel [19], Fabry [20], Rauber and Nesbitt [21] and Ryzhkov and Zrnic [22]. Other studies provide a systematic evaluation of the effect of different correction or retrieval algorithms on radar QPE, e.g., [23,24].

2.3.2 Clutter removal

Next, the radar reflectivity factor data from individual scans, together called the 3D or volumetric radar data, can be corrected for sources of error, which are related to environmental conditions and limitations in the scanning and sampling strategy. Some of the most important ones are discussed here. First, remaining non-meteorological echoes, called clutter, can be removed (Chapter 11 of Volume 1). Clutter can be caused by obstacles near a radar site or interference (Chapter 6 of Volume 3; [27]). Clutter can also be a result of reflections by airborne non-meteorological targets, such as aircraft and birds. A common cause of clutter is anomalous propagation: refraction of the beam towards the Earth's surface in case of specific temperature and/or moisture gradients in the atmosphere. Especially non-stationary targets, such as waves, ships and wind farms, are difficult to remove by Doppler filtering. Clutter can be a serious problem for QPE, since it can lead to large overestimation of precipitation.

Often, additional methods are needed to further reduce non-meteorological echoes. Many studies employ fuzzy logic algorithms involving single-polarisation and/or dual-polarisation decision variables [28–32]. Dual-pol radars are especially effective in detecting clutter. In contrast to hydrometeors, non-meteorological scatterers often have an irregular surface, which can be detected by comparing the amplitude and phase between horizontally and vertically polarised backscattered signals provided by dual-pol radars. This can be followed by statistical

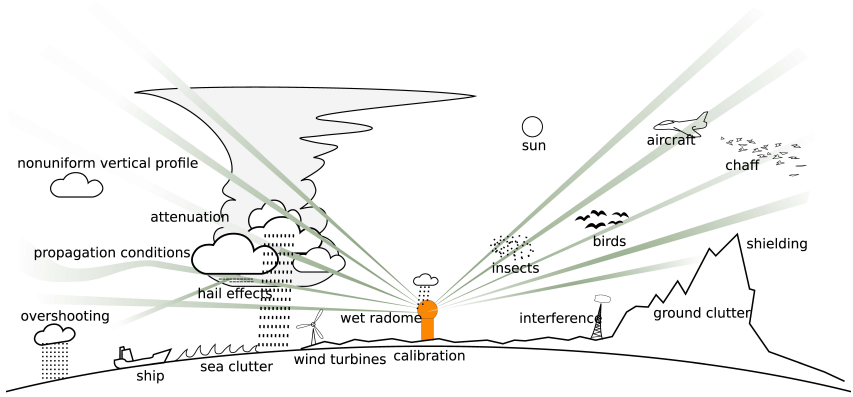

Figure 2.5 Overview of sources of error affecting QPE with ground-based weather radars. Reproduced with permission from Markus Peura (Finnish Meteorological Institute).

postprocessing, e.g., by creating clutter maps based on unrealistically large or frequent accumulations [33] or by detecting large spatial gradients in radar reflectivity factors and by removing isolated echoes [34]. Also auxiliary data are used to remove clutter, e.g., satellite cloud type [35], or precipitation probability products [36], or a combination of satellite and numerical weather prediction model data [37,38].

2.3.3 Attenuation correction

Precipitation can be severely underestimated due to rain-induced attenuation along the radar beam and wet radome attenuation for X- or C-band radars [39–44], especially in case of heavy, convective precipitation. This is illustrated in Figure 2.6 for two C-band radars. The squall line at 16:45 UTC (Universal Time Coordinated) moves in north-easterly direction over the Netherlands but almost completely disappears at 17:00 UTC, because the radar beams are aligned with the

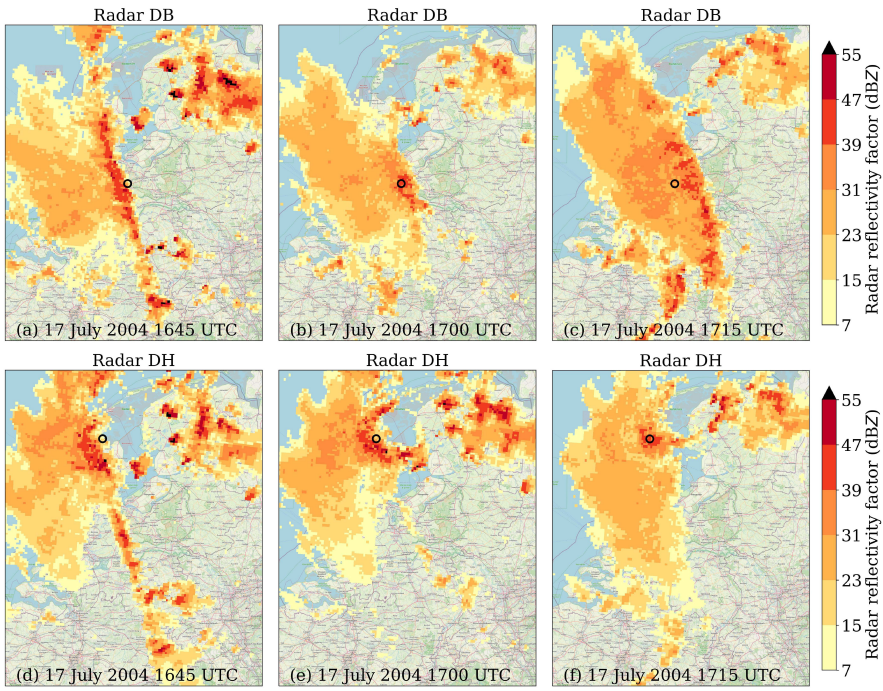

Figure 2.6 Example of severe (radome) attenuation. Maps covering the Netherlands and surroundings with the horizontally polarised radar reflectivity factor from the 800-m pseudo-CAPPI from the inland radar in De Bilt (DB; a–c) and the coastal radar in Den Helder (DH; d–f) and for 17 July 2004 16:45 (a,d), 17:00 (b, e) and 17:15 (c, f) UTC. Radar locations are denoted by black circles. Map data ©OpenStreetMap contributors 2023. Distributed under the Open Data Commons Open Database License (ODbL) v1.0.

squall line. For one radar, it reappears at 17:15 UTC (Figure 2.6(a)–(c)), because the radar now looks sideways to the squall line, i.e., the total path of two-way propagation through severe rain is much reduced. Given the fairly high radar reflectivity factor values above the radars, wet radome attenuation likely contributes to reducing the received radar reflectivity factor values. Algorithms can be applied to estimate the two-way path-integrated attenuation along the radar beam and correct for this. Hitschfeld–Bordan type algorithms convert Z or R to specific attenuation k using a power–law. Next, for each azimuth, k is integrated over the range of the beam. Hence, the attenuation is computed for each range bin and added to the radar reflectivity factor to correct for rain-induced attenuation in an iterative procedure [39,43,45]. To avoid numerical instabilities that can occur when applying Hitschfeld–Bordan type algorithms, constraints can be applied for a maximum allowed correction [43]. Alternatively, a similar algorithm can be applied, but in the reverse direction, using the estimated path-integrated attenuation to a fixed target as an additional constraint [45,46]. For dual-pol radars, the specific differential phase (K_{dp}) can be used as an independent variable to compute the path-integrated attenuation [47]. In that case, k is computed from K_{dp} using, e.g., a linear relationship. This can improve QPE with respect to a Hitschfeld–Bordan type algorithm [44]. Wet radome attenuation correction has received little attention in the scientific literature, e.g., [48–50].

2.3.4 Vertical profile of reflectivity correction

Shallow precipitation and orographically enhanced precipitation at longer ranges from the radar can be (partly) missed due to the increased height of the radar sampling volume ('overshooting'). Moreover, stratiform precipitation starts as (dry) snowflakes and ice crystals resulting in low reflectivities higher up, via a layer with higher reflectivities due to melting snow ('the bright band', on radar reflectivity or precipitation images often visible as circles with increased values around the radar site), to moderate reflectivities due to rain below the melting layer. The vertical profile of reflectivity can be estimated close to the radar site using data from multiple elevation scans and can subsequently be used to correct for the low reflectivity at long ranges from the radar [51].

2.3.5 Conversion to rainfall intensity

At the core of radar QPE is the conversion of the horizontally polarised radar reflectivity factor Z to rainfall intensity R (Chapter 6 of Volume 2; [12]). The most widely used relation is given by $Z = 200R^{1.6}$, which was obtained from raindrop size distribution observations at the ground [52], and is often used in temperate climates. The values of the coefficients may vary considerably between rainfall types, implying that a fixed $Z-R$ relationship introduces (large) uncertainties [53]. Hence, sometimes different coefficients are employed depending on the value of Z. Dual-pol radars provide opportunities to improve QPE (Chapter 5 of Volume 2). For instance, in case of moderate or stronger rainfall, the dual-pol variable specific differential phase (K_{dp}) can be employed for rainfall estimation. Advantages are that it is immune

for hardware calibration errors, (radome) attenuation and partial beam blockage, and that the $K_{dp}-R$ relationship introduces less uncertainty because it is not as non-linear as the $Z-R$ relationship. It can only be applied in rain, however, requiring a hydrometeor classification algorithm or temperature information from weather models to determine whether K_{dp} can be used for QPE or not.

Applying the $Z-R$ relationship assumes that precipitation is liquid. Although rainfall is the dominant precipitation type at the Earth's surface for most areas covered by radars, aloft the radar often measures the backscatter by solid precipitation or mixtures of precipitation. Applying a $Z-R$ relation for liquid precipitation then results in an underestimation of surface rainfall (except for hail). Here, hydrometeor classification algorithms [54–56] can help to select appropriate relationships to convert either Z, Z and the differential reflectivity Z_{dr} (Chapter 5 of Volume 2), or K_{dp}, to rainfall intensity or to even estimate the surface snowfall intensity.

2.3.6 Radar-gauge adjustment

Typically, data from different radars are combined in 2D reflectivity or precipitation fields to obtain better estimates. A common practice is to complete the radar processing chain by adjusting 2D radar precipitation fields using near real-time or historical rain gauge accumulations [59–65]. This entails the computation of an adjustment factor for each radar grid cell (pixel) and applying this factor to the unadjusted radar data. This can be a constant factor over the entire radar domain, a so-called mean-field bias adjustment, or a spatial adjustment factor which can vary from grid cell to grid cell. Adjustment is called merging in case an adjustment factor field is computed using rain gauge and radar data from the same, typically 60 min or 24 h, interval and subsequently applied to the radar data from that interval. When no recent rain gauge data are available, an adjustment factor field can be computed based on historical radar and gauge data and applied to radar data from the present time interval [64,66]. Typically, for each rain gauge location, the ratio of gauge and radar accumulations is computed. For a given radar grid cell, the ratios from surrounding gauge locations are interpolated to obtain an adjustment factor value, where the ratios from the nearest gauge locations get the highest weight. Alternatively, first the radar and gauge values at rain gauge locations are interpolated separately through distance-weighting. The ratio of these values for a given radar grid cell gives an adjustment factor value. An overview of several common gauge adjustment methods is provided by Goudenhoofdt and Delobbe [67]. A practical limitation for merging rain gauge data in real-time radar products is the latency of rain gauge measurements [66]. Gauge-adjusted radar precipitation products are, e.g., highly relevant for radar hydrology (Chapter 1 of Volume 3).

An example of a merged radar-gauge dataset is the 25-year climatology of annual precipitation for the Netherlands presented in Figure 2.7, which is based on the methodology by Overeem *et al.* [17]. Such climatological radar precipitation datasets [68] also exist for, e.g., Germany [69], Europe [35] and the United States of America [70]. For the unadjusted radar dataset, algorithms to improve QPE are mainly limited to Doppler clutter filtering and some statistical clutter removal algorithms. The highest accumulations are caused by clutter resulting from anomalous propagation

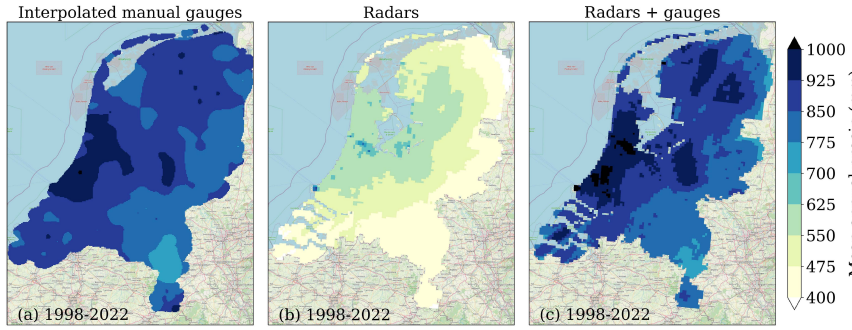

Figure 2.7 Maps of mean annual precipitation for the Netherlands for the period 1998–2022, based on interpolated rain gauge data [57] (a), unadjusted radar data (b) and gauge-adjusted radar data [58] (c). Availability is 91.0% for the radar datasets, which is taken into account when computing the mean annual precipitation (map data ©OpenStreetMap contributors 2023. Distributed under the Open Data Commons Open Database License (ODbL) v1.0).

and occur in an area part of the Port of Rotterdam, where many metal cranes and containers are located. The huge underestimation (Figure 2.7(b)) with respect to the interpolated rain gauge dataset (Figure 2.7(a)) is effectively removed by merging with data from KNMI's rain gauge networks (Figure 2.7(c)). This provides a much more detailed perspective on local precipitation, confirming the added value of gauge-adjusted radar accumulations for climate monitoring. For some azimuths pointing away from radar locations, clearly lower accumulations are found. These can be related to obstacles, in this case mostly buildings or orography, near radar sites that partly block the beam of the lowest elevation scan. Algorithms are available to recognise and correct for beam-blockage affected areas using digital elevation models, by employing specific differential phase or by employing specific attenuation [71–73], and can be applied when 3D radar data are available.

2.3.7 Evaluation

Now a more quantitative assessment of the quality that can be expected from (gauge-adjusted) radar precipitation products is provided in Figure 2.8. Daily radar rainfall accumulations are evaluated against KNMI's manual rain gauge network over a period of almost 1 year. Four different datasets are evaluated as follows:

- A dataset obtained with similar methods as the unadjusted radar dataset from Figure 2.7 ('no radar corrections'). Note that data from the two radars are averaged in logarithmic space, to limit the effect of clutter [74].
- A dataset which has undergone clutter removal with a fuzzy logic algorithm [74], attenuation correction via K_{dp} [44], vertical profile of reflectivity correction [51], quality-based conversion of 3D to 2D data per radar, clutter removal by a statistical filter [34], quality-based compositing of data from the

two radars, and advection correction to account for fast moving precipitation ('radar corrections'). Data from the two radars are averaged in linear space, which can be done because of the effective clutter removal. This reduces underestimation compared to averaging in logarithmic space [74].

- For both datasets also a spatial gauge adjustment is performed using 1-h accumulations of KNMI's automatic rain gauge network. Given limitations in latency and update frequency of automatic rain gauge data, such an adjustment is not always possible in real-time.

A number of conclusions can be drawn from Figure 2.8. First, the average underestimation is severe without gauge adjustment, even when radar corrections are applied. This underlines that more radar corrections are needed and that gauge adjustment is still desirable for operational applications. Second, the gauge adjustment using only ∼1 gauge/1,000 km^2 is more effective in improving QPE than radar corrections alone. Third, radar corrections further improve the gauge-adjusted radar accumulations. To conclude, the effect of radar corrections is relatively limited but noticeable.

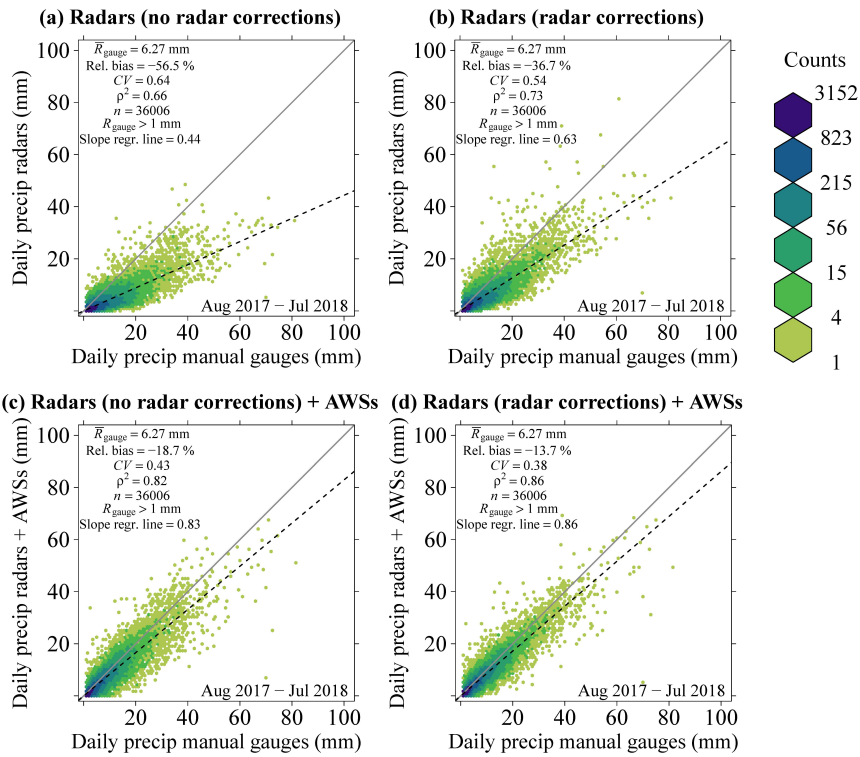

Figure 2.8 Evaluation of four radar datasets with ∼0.9 km^2 grid cells against daily manual rain gauge point accumulations over ∼1 year. For unadjusted (a, b) and adjusted (c, d) radar data. For this comparison, the radar grid cell at each gauge location is employed.

Note that Figure 2.8 only provides a general evaluation. The outcome could be different when considering hourly accumulations, other evaluation metrics or specific events. For instance, annual precipitation maps (not shown) reveal that the radar corrections lead to more realistic, substantially higher accumulations at long range from the radars, where no KNMI rain gauges are present. Figure 2.8 gives an impression of the quality of (gauge-adjusted) radar QPE one may encounter. The actual performance may be lower or higher for other radar networks, depending on, e.g., environmental conditions, hardware (calibration), applied (additional) radar corrections and density of employed rain gauge networks. Finally, representativeness errors explain part of the variability between radar and gauge accumulations [75]. Radars measure aloft and sampling volumes are huge compared to the typical 2–4 dm^2 sampling area of rain gauges, which measure at the Earth's surface. Because of representativeness errors, the minimum accumulation period for comparing or merging rainfall estimates from radar and rain gauges is usually assumed to be 60 min. This reduces the impact of rainfall variability.

2.4 QPE with personal weather stations

2.4.1 Quality control

It is expected that rain gauge data from PWSs are more prone to errors due to placement at sites with more interference from the surroundings, fewer and less-specialised maintenance to the sensor and lower quality devices compared to AWSs. QC methods have been developed to recognise typical errors in this data source and are commonly applied to PWS rain gauge data. These algorithms are sometimes available as open-source algorithms [82,84,86–88]. Often, inter- and/or intra-station checks are performed, and sometimes auxiliary data from, e.g., government rain gauges [82] or radar data [89] are used. Inter-station filters make use of the fact that rainfall is correlated in space [90]. Applying QC can substantially decrease the number of observations. Here, previously developed QC [84,91] is applied to 6 months of Netatmo PWS data from the Netherlands (the data from March to May 2020 are used as spin-up time). After obtaining precipitation accumulations at regular 5-min intervals, a list of all nearest PWSs (up to a maximum of 20) within a 10-km radius is compiled for each PWS, which feeds into the inter-station QC.

Box 2.3: Introduction to PWSs

PWSs are typically purchased by weather enthusiasts or citizen scientists and are often located in densely populated areas. PWSs provide observations in urban areas where AWSs are relatively scarce due to the difficulty to meet WMO requirements. Common PWSs are produced by companies such as Alecto, Davis and Netatmo. The Netatmo PWS consists of an indoor and outdoor module, with the possibility to extend with an additional outdoor module for rain and an outdoor module for wind [76]. The rain module is of the tipping bucket type and the observations are sent to the Netatmo platform every ~5 min and are visualised on

the Netatmo Weathermap (https://weathermap.netatmo.com/). Several other platforms exist to which data from a variety of PWSs are uploaded, such as the Weather Observations Website (free access; https://wow.metoffice.gov.uk/; https://wow.knmi.nl/) [77–79], the Weather Underground website (https://www.wunderground.com/wundermap) [78] and the Community Collaborative Rain, Hail and Snow Network (https://www.cocorahs.org/) [80]. The quality of PWS sensors, the set-up in relation to the often urban environment, metadata, connectivity, data transfer, power supply, calibration and maintenance are of vital importance for rainfall estimation [81–83]. Typical sources of error in (PWS) rain gauge estimation are discussed by De Vos *et al.* [81,84] and Ośródka *et al.* [85] and references therein.

The algorithm distinguishes [84]

- faulty zero errors caused by malfunctioning of the gauge (e.g. a failing tipping bucket mechanism);
- high influx errors, which are suspiciously large accumulations that may be caused by, e.g., garden sprinklers and tilting of the gauge while handling the device or signal processing errors (e.g. values are added upon previous observations);
- station outlier errors where observed rainfall dynamics do not correspond with those at nearby PWSs;
- bias due to systematic underestimation or overestimation that may be caused by wind or a deviating tipping bucket volume, either physically or due to faulty calibration.

The faulty zeroes, high influx, and station outlier filters and dynamically updated bias correction factors are computed and applied to the 5-min data. Given the spin-up time needed for the station outlier filter and bias correction, only QPE from the most recent 3 months is evaluated. Note that the bias correction starts with a default bias correction factor (1.09), which has been obtained from a one-of comparison to gauge-adjusted radar data from September 2019 [92]. Apart from this default bias correction factor, the default parameters have been obtained from De Vos *et al.* [84], who employ an older Netatmo rain gauge dataset from the Amsterdam metropolitan area, the Netherlands. For each PWS, the QC'ed 5-min accumulations are aggregated to hourly and daily point accumulations in case the availability is at least 83.3%. The hourly point accumulations are interpolated at the $\sim$0.9 km^2 radar grid using ordinary kriging with a spherical variogram model [93] employing the RAINLINK software package and its default parameter values [94]. Climatological variogram parameters are used, which vary as a function of day of year, and which are based on a 30-year rain gauge dataset [90]. The 1-h PWS rainfall maps are aggregated to 24-h and 3-monthly rainfall maps.

2.4.2 Evaluation

Interpolated PWS 3-monthly rainfall maps are compared to gauge-adjusted radar precipitation maps (Figure 2.9(a) and (b)). The spatial patterns and values of

3-monthly PWS summer precipitation match well with the gauge-adjusted radar dataset. As expected, more detailed patterns are visible in the radar precipitation map, and local extremes are missed by the PWS network, which may be partly caused by the limited PWS coverage. No clear outliers are visible for the PWSs. Interpolated daily PWS rainfall maps and daily PWS point rainfall estimates are validated against KNMI rain gauge point accumulations and gauge-adjusted radar accumulations, respectively (Figure 2.9(c) and (d)). The scatter density plots show

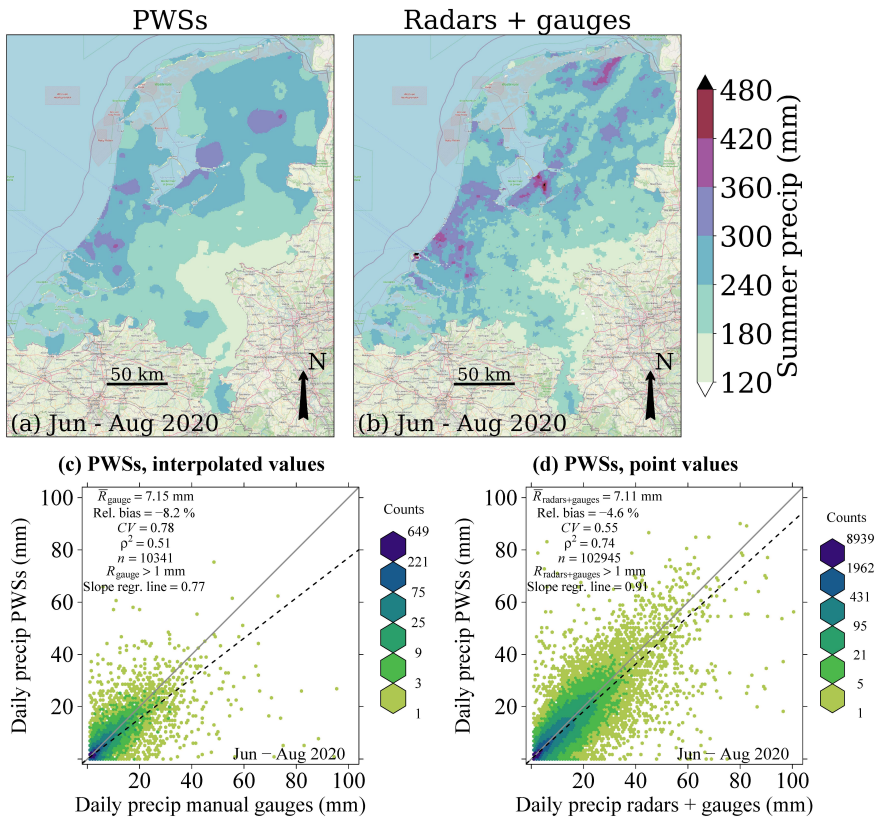

Figure 2.9 Comparison of 3-monthly interpolated PWS precipitation accumulation map (a) against gauge-adjusted radar accumulation map [95] (b) at ∼0.9 km² for the period 31 May 2020 08:00 UTC to 31 Aug 2020 08:00 UTC. Evaluation of interpolated daily PWS rainfall accumulations against manual rain gauge point accumulations over the same period (c), and evaluation of PWS point accumulations against gauge-adjusted radar accumulations with ∼0.9 km² grid cells [96] over the same period (d). For the PWS point accumulation comparison, the radar grid cell at each PWS location is employed. Map data ©OpenStreetMap contributors 2023. Distributed under the Open Data Commons Open Database License (ODbL) v1.0.

that the relative bias is within 10%, the dispersion is relatively low (CV<1), and the value for ρ^2 is moderate (interpolated maps) to large (point values). Clearly better results are obtained for the comparison of PWS point values with gauge-adjusted radar data than for interpolated PWS maps against manual rain gauge data. The interpolation of PWS values introduces mapping errors. These are absent for the PWS point values, although the comparison with radar data introduces representativeness errors. This suggests that, for the given PWS network density, mapping errors are more important than errors due to radar-PWS representativeness differences.

2.5 QPE with commercial microwave links

2.5.1 Sources of error and processing chain

MNOs typically store signal level data in their network management systems every 15 min. The workflow for CML rainfall retrieval starts with coupling of metadata (link locations, path length, microwave frequency and optionally polarisation) and data (received and optionally transmitted signal levels), if not done already by the MNO. Preprocessing may be needed, e.g., to detect errors in metadata or to only select CMLs with certain microwave frequencies. An important source of error from the perspective of QPE is that signal levels can also decrease during dry periods, e.g., due to reflection or refraction of the beam, changed antenna patterns, dew formation on the antennas, or dust [101,104–107]. Hence, a commonly applied next step is a wet–dry classification that results in zero retrieved rainfall intensities for dry periods. This is an important step to improve CML QPE, also because it contributes to determining an accurate reference signal level, representative for dry periods [18,107,108]. Such a wet–dry classification typically uses intra- [109] or inter-station checks. Sometimes auxiliary radar [18] or satellite [110] data are employed. In this section, an inter-station check is performed by employing the mutual decrease in received signal levels from neighbouring sub-links [18,93]. The basic principle behind such inter-station methods is that rainfall is correlated in space. Another source of error is attenuation due to wet antennas, which may result in overestimation of the rain-induced attenuation along the path. Wet antenna attenuation correction is commonly applied [18,111–115]. Finally, the CML rainfall estimates are often interpolated to obtain rainfall maps, which introduces mapping errors [116]. More information on sources of error in CML rainfall retrieval and algorithms to account for these are provided by Overeem *et al.* [93,107] and Graf *et al.* [117].

Box 2.4: Introduction to CMLs

CMLs are close to the ground radio connections used globally as backhaul in cellular telecommunication networks. Along such links, radio signals

propagate from a transmitting antenna at one base station (telephone tower) to a receiving antenna at another base station.

CML illustration by identim/Shutterstock

CMLs operate at frequencies where raindrops substantially attenuate radio waves due to scattering and absorption [97–99]. The International Telecommunication Union's traditional frequencies in the range from 6 to 42 GHz are the most widely used worldwide and will remain very important in the coming years [5]. A CML often has two sub-links for communication in both directions. For each sub-link, the path-averaged rainfall intensity can be retrieved from the signal's attenuation between transmitter and receiver. For constant transmitted signal levels, this rain-induced signal attenuation is computed by subtracting the received signal level from a reference received signal level, being representative for dry periods. In case transmitted signal levels vary, the attenuation is computed by subtracting received signal levels from transmitted signal levels and subtracting these from a reference level (base level; also computed by subtracting received from transmitted signal levels). The core of CML rainfall retrieval is based on a power–law between path-averaged rainfall intensity and specific attenuation (dB km^{-1}) [98,99]. The coefficients of this power–law are derived from observed drop size distributions and simulations of electromagnetic scattering by raindrops [100] and primarily depend on carrier frequency and polarisation of the signals. Overviews on the history and physics of CML rainfall retrieval are provided by Messer and Sendik [101], Uijlenhoet *et al.* [102] and Chwala and Kunstmann [103].

Since approximately 2005, the potential of CML rainfall monitoring has been shown in many publications, e.g., for the Czech Republic [118], Germany [105,117], Israel [119,120] and the Netherlands [107,112,121,122]. Common sampling strategies provide minimum and maximum, average, or instantaneous received (and transmitted) signal level data. These introduce uncertainties, e.g., by estimating 15-min averaged rainfall intensities from minimum and maximum rainfall intensities. Alternatively, an open-source CML data acquisition system could be set up, which allows for real-time sampling every minute or better [123,124].

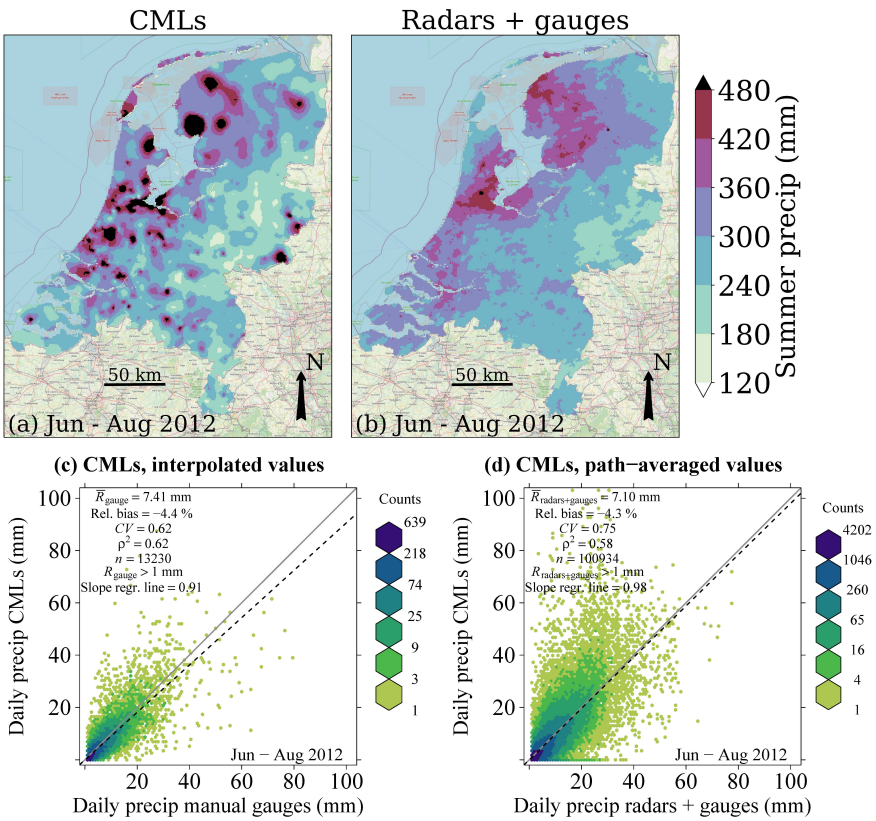

Figure 2.10 Comparison of 3-monthly interpolated CML precipitation accumulation map (a) against gauge-adjusted radar accumulation map [95] (b) at ∼0.9 km² for the period 31 May 2012 08:00 UTC to 31 August 2012 08:00 UTC. Evaluation of interpolated daily CML rainfall accumulations against manual rain gauge accumulations over the same period (c) and evaluation of CML path-averaged accumulations against the corresponding path-averaged gauge-adjusted radar accumulations [96] over the same period (d) (map data ©OpenStreetMap contributors 2023. Distributed under the Open Data Commons Open Database License (ODbL) v1.0).

Here, a Dutch dataset of minimum and maximum received signal levels over 15-min intervals is used. Carrier frequencies range from 13 to 40 GHz. The majority of CMLs are shorter than 5 km. The RAINLINK software package (Version 1.3) for CML rainfall retrieval and mapping is applied to obtain 15-min path-averaged and interpolated CML rainfall estimates for the $\sim$0.9 km^2 radar grid covering the land surface of the Netherlands [93,125]. RAINLINK's default parameter settings [93] are employed and the same interpolation method as for the PWSs. The 15-min CML rainfall maps are aggregated to 24-h and 3-monthly rainfall maps. For each CML, the 15-min rainfall intensities are aggregated to hourly and daily path-averaged accumulations in case the availability is at least 83.3%.

2.5.2 Evaluation

Interpolated CML 3-monthly rainfall maps are compared to gauge-adjusted radar precipitation maps (Figure 2.10(a) and (b)). The spatial patterns and values of 3-monthly CML summer precipitation are in reasonable agreement with the gauge-adjusted radar dataset but also show underestimation in the east, and many local outliers. Interpolated daily CML rainfall maps and daily CML path-averaged rainfall estimates are validated against KNMI rain gauge point accumulations and path-averaged gauge-adjusted radar accumulations, respectively (Figure 2.10(c) and (d)). The scatter density plots show that the relative bias is within 10%, the dispersion is relatively low (CV$<$1), and the values for ρ^2 are quite large. Despite shortcomings in CML rainfall estimations, their overall performance is quite good, certainly when one realises that CMLs have not been designed for rainfall estimation and that part of the deviations in CML rainfall estimates are related to mapping or representativeness errors.

2.6 Summary and outlook

An overview was provided of the required and possible processing steps for rainfall estimation with ground-based weather radars, PWSs and CMLs. Sources of error and algorithms to remedy these were presented. The quality of (gauge-adjusted) radar, PWS and CML datasets was evaluated for the Netherlands. Despite several processing steps being applied to radar data, adjustment with rain gauge data remains important to improve radar QPE. Opportunistic sensors were shown to provide useful complementary precipitation information, but sensor quality, quality of set-up (PWSs) and network densities (CMLs, PWSs) could decrease over time. Hence, government rain gauge networks, including those from water authorities, remain important, also for purposes requiring consistent observations at the highest accuracy, such as climate trend analyses. Also public rain gauges, e.g., from universities, may add value. Note that government and public rain gauges may not always follow WMO guidelines and may need additional QC, similar to PWSs. Other opportunistic sensors, such as satellite microwave links (SMLs) between Earth and space [13,126], can potentially provide additional precipitation information. Signals between satellites and satellite receiver terminals at the ground,

often used for digital video broadcasting, are attenuated by rain. Similarly to CMLs, these signals can be converted to path-averaged rainfall rates, but over a slant path through the atmosphere from the Earth's surface towards the satellite instead of near the Earth's surface and parallel to it.

The CML rainfall maps outperform the PWS rainfall maps when compared to rain gauges, possibly because of the larger physical footprint of CMLs resulting in more rainfall events being captured. It is the other way around for the point or path-averaged values when compared to gauge-adjusted radar accumulations, which suggests that the PWS sensor is more accurate than the CML sensor. A disadvantage of the CML with respect to the PWS rainfall maps is the many outliers found in the 3-monthly accumulations. An exact comparison is not possible due to the different periods for the CML and PWS data.

2.6.1 Merging opportunistic sensing and radar data

Due to the often large spatial variability in sources of error in radar QPE (e.g. due to attenuation), especially errors generally becoming larger at longer distance from a radar due to larger sampling volumes higher above the Earth's surface, it is probably more effective to improve radar QPE by merging with less accurate opportunistic sensors from a high-density network than by merging with data from highly accurate AWSs from a much sparser network. This is confirmed below.

Merging of PWS rain gauge with radar precipitation data has been suggested by [127] and is one of its most important use cases. Merging is feasible when coverage of radar and PWS (Figure 2.1(a) and (d)) is both dense, which happens to be the case in high-income countries. In the, to the best of our knowledge, first study investigating radar-PWS merging, a full year of pan-European 1-h radar accumulations is merged with PWS rain gauge accumulations from Netatmo employing a spatial adjustment method [89]. Evaluation against government rain gauges from ECAD [8,9] confirms that the quality of radar QPE is much improved compared to the unadjusted radar dataset but has lower quality than the climatological radar dataset EUropean RADar CLIMatology (EURADCLIM) [89]. In the EURADCLIM dataset, radar accumulations from OPERA (Operational Program on the Exchange of Weather Radar Information) are merged with rain gauge accumulations from ECAD [35]. The averaging of PWS-gauge values by merging also seems to act as a form of QC. The large number of locations of the PWS dataset is expressed by the median number of employed radar-gauge pairs in the merging. It is $\sim$6 times larger for the PWS gauges compared to the ECAD gauges. The underestimations found for lower temperatures point to solid precipitation being missed by Netatmo PWSs due to the absence of a heating device [89].

Here, the 3-monthly QC'ed PWS dataset from the Netherlands is merged with KNMI radar precipitation accumulations. The QC and merging algorithms from Overeem *et al.* [89] are applied: the faulty zeroes and high influx filters, the station outlier filter and dynamically updated bias correction from [84] fed with a default bias correction factor of 1.09 [92] (not applied in [89]), QC with unadjusted radar data (after which [89] apply a default bias correction factor of 1.06), and a spatial adjustment on 1-h accumulations based on Barnes' objective analysis [128]. For

each radar grid cell, such a spatial adjustment factor is computed from the ratio of the distance-weighted interpolation of unadjusted radar accumulations and the interpolation of the corresponding gauge precipitation accumulations from all selected radar-gauge pairs. The 1-h merged radar-PWS dataset is aggregated to daily accumulations and compared to KNMI's manual rain gauge accumulations in Figure 2.11(c). The large underestimation in the unadjusted radar dataset (Figure 2.11(a)), which involves no radar corrections (Section 2.3.7), is largely removed. The merged radar-PWS accumulations in Figure 2.11(c) are much closer to the 1:1 line, also for extremes. On average, accumulations from 118 PWS locations are employed in the merging (much lower than the total number of PWSs, mainly because radar-gauge pairs are only employed in the merging process when their unadjusted radar and PWS 1-h values are both larger than 0.25 mm). The radar-PWS dataset outperforms the radar-AWS dataset (Figure 2.11(b)), which uses rain gauge data from 32 locations. It is apparent that the underestimation is still quite large for the radar-AWS dataset compared to the unadjusted radar dataset.

Spatial patterns are captured by the radar-PWS dataset (Figure 2.12(c)). Although values are much more realistic than for the unadjusted radar dataset (Figure 2.12(a)), the comparison with the climatological gauge-adjusted radar dataset also reveals strong underestimation (Figure 2.12(d)). For the radar-AWS

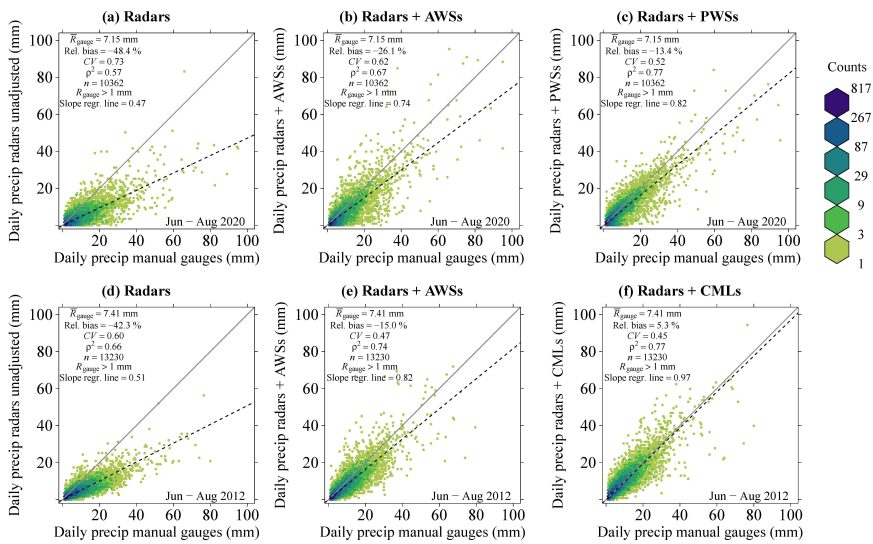

Figure 2.11 Evaluation of (merged) daily radar precipitation accumulations with ~0.9 km^2 grid cells against manual rain gauge point accumulations. For unadjusted radar data (a, d), radar data adjusted with rain gauges from AWSs (b, e) and for radar data adjusted with opportunistic sensing data (c, f). Note that the 3-monthly periods for PWSs and CMLs are from a different year. For these comparisons, the radar grid cell at each gauge location is employed.

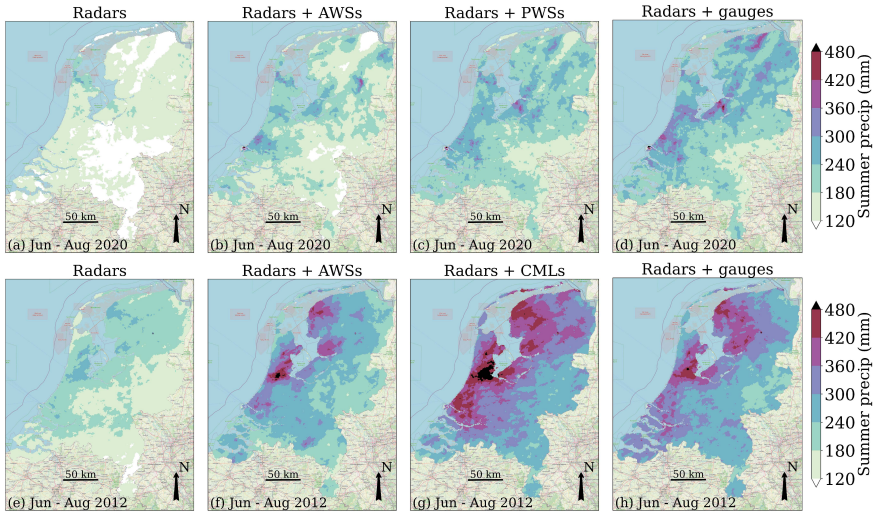

Figure 2.12 Evaluation of (merged) 3-monthly radar precipitation maps with ~0.9 km^2 grid cells. For unadjusted radar data (a, e), radar data adjusted with rain gauges from AWSs (b, f), and radar data adjusted with opportunistic sensing data (c, g). The fourth column presents the climatological radar dataset [95], where automatic and manual KNMI rain gauges are merged (d, h). Note that the 3-monthly periods for PWSs and CMLs are from a different year. Map data ©OpenStreetMap contributors 2023. Distributed under the Open Data Commons Open Database License (ODbL) v1.0.

dataset locally some suspiciously high accumulations are found in the north-east (Figure 2.12(b)), pointing to instabilities in the merging algorithm (due to the sparse AWS network) or local showers only captured by the AWSs. Such an outlier may be caused by severe underestimation by radars at gauge locations, resulting in too large adjustment factors in other grid cells for which the underestimation is less severe. In particular, strong spatial rainfall gradients and fast-moving showers around rain gauge locations can result in a mismatch between radar and gauge values due to representativeness errors. Outliers are not found for the radar-PWS dataset, which confirms the quality of the underlying PWS data and the performance of the applied QC.

Some successful initial work on radar-CML merging has been performed [129,130]. Others investigate rainfall mapping based on CML and gauge data [131,132]. The combined worldwide radar-CML coverage shows that radar-CML merging could be feasible in many middle- and high-income countries (Figure 2.1(a) and (e)). Now, the 3-monthly CML dataset from the Netherlands is merged with KNMI radar precipitation accumulations. The 15-min path-averaged rainfall intensities are aggregated to 1-h CML rainfall accumulations in case of full

availability. The corresponding path-averaged unadjusted radar accumulations are extracted. As for the PWS data, QC with unadjusted radar data is performed. From the path-averages of radar-CML pairs, to which the coordinates of the middle of the link path are assigned, a spatial adjustment factor field is computed following the same methodology as for the PWS accumulations. The 1-h merged radar-CML dataset is aggregated to daily accumulations and compared to KNMI's manual rain gauge accumulations in Figure 2.11(f). The large underestimation found for the unadjusted radar dataset (Figure 2.11(d)) turns into a small overestimation by the radar-CML merging, with clearly better values for CV and ρ^2. On average, accumulations from 72 CML locations are employed in the merging (much lower than the total number of CMLs, mainly because radar-CML pairs are only employed in the merging when their unadjusted radar and CML 1-h values are both larger than 0.25 mm). The radar-CML dataset outperforms the radar-AWS dataset (Figure 2.11(e)), especially in terms of the relative bias (note that 0.25 mm thresholding on radar-gauge pairs has not been applied for all radar-AWS datasets in this chapter). The spatial comparison in Figure 2.12(g) and (h) with respect to the climatological gauge-adjusted radar dataset reveals overestimations for several areas. Spatial patterns are well captured except for the eastern part of the Netherlands. The outliers that are present in the CML-only map (Figure 2.10(a)) are not found in the radar-CML dataset, except for an area with suspiciously high accumulations in the west. The merging seems to act as an additional QC. This area, albeit much smaller, is also present in the radar-AWS dataset. To conclude, radar-CML merging helps to remove systematic underestimations and provides better rainfall estimates than radar-AWS merging for the employed AWS and CML network densities.

Although a fair comparison between the performance of the radar-PWS and radar-CML dataset is not possible given the different periods and the differing network densities, the radar-CML merging seems more promising for improving radar QPE. This is unexpected due to the fact that PWSs provide a more direct observation in contrast to the indirect remote sensing by CMLs, and because the number of pairs in the merging is on average higher for PWSs (118) than for CMLs (72). One explanation is that the majority of CMLs in this study are at most a few kilometres long, which reduces representativeness errors with respect to radar estimates compared to PWSs and to longer CMLs. This also implies that CMLs capture a much wider area compared to PWS point observations, which can help to capture more events, although their intensities may be lower than from local (PWS) point observations.

In this chapter, only summer precipitation, dominated by rain, was discussed. One limitation of these opportunistic sensing data is that detection of solid precipitation is often limited (PWSs) or not possible (CMLs), and that melting precipitation leads to overestimation for CMLs [107,133]. Apart from this limitation, the high network densities of PWSs and CMLs compared to AWSs, the potential (near) real-time availability of PWS and CML data, and the performance of merged radar-PWS and radar-CML datasets, suggest that (real-time) radar precipitation products could benefit from these opportunistic sensing data. Also note that latency and update frequency of automatic rain gauge data could hamper real-time radar-AWS merging. Instead, a spatial adjustment factor from the previous hour could be

used for the present hour, which will result in (slightly) worse rainfall estimates for the 'Radar + AWSs' dataset. Note that the added value of the PWS and CML datasets has been tested on a radar dataset which has been subjected to only a few correction algorithms (i.e. no attenuation correction and no vertical profile of reflectivity correction). The impact of employing opportunistic sensing data for improving radar QPE is expected to be less for more thoroughly processed radar datasets. Also note that in reality AWS rain gauge data are often available with some delay (1–60 min), which prevents real-time merging of AWS and radar data from the same and most recent time interval. The latency of CML data, provided that a real-time data acquisition system is used [123], and PWS rain gauge data may be shorter.

Development of operational radar products incorporating PWS or CML rainfall data, optionally including AWS data, is already being studied by some NMHSs in Europe [130]. Since radar QPE feeds into nowcasting and seamless forecasting systems [134], merged radar opportunistic sensing datasets can contribute to improved monitoring of severe weather and warnings for potential (flash) floods and landslides.

2.6.2 CMLs as 'weather radars' for the tropics

Several studies address CML rainfall estimation in (sub)tropical climates, namely for Burkina Faso [106], Kenia [135], Brazil [136], Pakistan [137] and Nigeria, Sri Lanka and Papua New Guinea [14,138]. Overeem *et al.* [139] show the great potential of CMLs for tropical rainfall monitoring based on a 3.5-month dataset of on average 1140 link paths from Sri Lanka when compared to government rain gauge data. Due to the absence of ground-based weather radars, a high-resolution and relatively accurate spatial verification of CML rainfall maps can only be performed employing the space-borne precipitation radar from the GPM mission. Figure 2.13 presents an example of a good match between a 15-min CML rainfall map and the snapshot from GPM's combined radar-radiometer precipitation product (Chapter 9 of Volume 2). GPM's core satellite only has roughly one overpass per day for a given location, whereas the CML-based rainfall maps could be available every 15 min. CML rainfall maps were shown to outperform geostationary and GPM Integrated Multi-satellitE Retrievals for GPM (IMERG) precipitation products for the Netherlands [140] and have generally higher spatial detail. This perspective from space also brings to mind that CMLs could be used for ground validation of satellite precipitation products in areas that lack sufficient surface rainfall observations. Eventually, this could lead to improved satellite precipitation retrieval algorithms or better calibration.

Ultimately, for areas without ground-based weather radars in LMICs, often in (sub)tropical regions, CMLs could be used as 'weather radars' and used for real-time rainfall monitoring and nowcasting up to a few hours in advance. For LMICs, installing and maintaining radars is often simply too expensive. CML nowcasting has been positively evaluated for the Netherlands, where relatively good reference data are available [141]. Eventually, the CML rainfall maps could be merged with satellite precipitation products, taking advantage of their much wider coverage. CML-based (nowcasting) rainfall products may feed into (urban) hydrological models, which has been evaluated for temperate climates [142–144]. This calls for upscaling CML

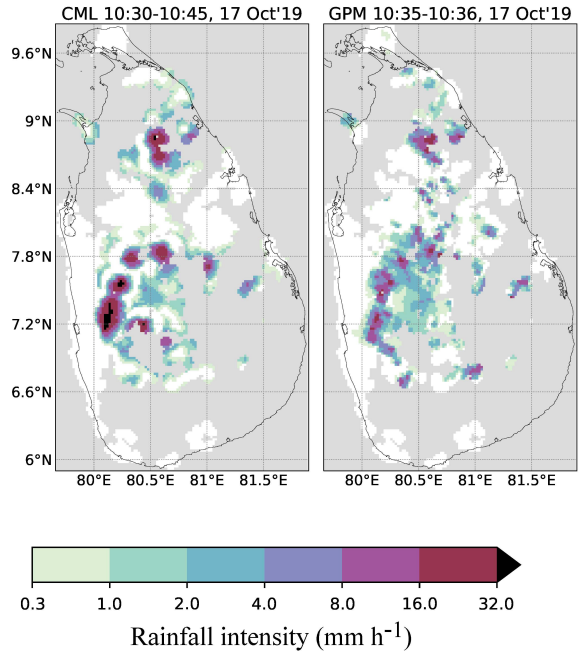

Figure 2.13 *A 15-min CML rainfall map (left) versus a satellite rainfall map from the GPM combined precipitation product (right; based on the GPM Combined Radar-Radiometer Precipitation Algorithm, version V06A) over Sri Lanka. Only combined CML-satellite coverage is plotted. Rainfall intensities smaller than 0.3 mm h^{-1} are white. Figure taken from [139].*

rainfall estimation in the Global South, for which Priebe [14] gives perspectives on use cases, business models and developing CML rainfall services and gives a showcase of a prototype of such a service. For new networks and countries, an evaluation covering at least six months of data with (a few) thousands of CMLs is recommended in order to develop a robust minimum viable product. Preferably, local climate and network characteristics are taken into account through rainfall retrieval parameter optimisation. One particular challenge for (sub)tropical regions is the lack of reference data needed to validate and optimise the CML rainfall retrieval. Ideally, local drop size distribution observations or those from a similar climate would be employed to compute representative coefficients for the power–law relationship between rainfall intensity and specific attenuation.

Acknowledgements

The locations of (GTS) rain gauges as used in GPCC products were kindly provided by Mr. Peter Finger, Mr. Udo Schneider and Dr. Andreas Becker (DWD; Deutscher

Wetterdienst). We thank Dr. Hylke E. Beck (King Abdullah University of Science and Technology, Saudi Arabia) for providing a radar reflectivity composite screenshot for Saudi Arabia. We thank the NMHS Met Norway for jointly purchasing the Netatmo rain gauge dataset. We acknowledge the private company Netatmo for providing the rain gauge data and for their cooperative attitude. This research would not have been possible without the commitment of the citizen scientists providing data from their Netatmo IoT rain gauge devices, which they bought, installed and maintained. We gratefully acknowledge Ronald Kloeg and Ralph Koppelaar from T-Mobile NL (currently known as Odido) for providing the cellular telecommunication microwave link data. We gratefully acknowledge our colleagues Linda Bogerd (Wageningen University & Research; Royal Netherlands Meteorological Institute) and Lotte de Vos (Royal Netherlands Meteorological Institute) for providing feedback on our manuscript. The constructive comments from two anonymous reviewers are appreciated. We thank the GSM Association, especially Jan Priebe, for their support for CML rainfall estimation in Sri Lanka. All figures containing maps were made with Python package Cartopy [145].

Abbreviations

AWS	automatic weather station
CML	commercial microwave link
CV	coefficient of variation
ECAD	European Climate Assessment and Dataset
EURADCLIM	EUropean RADar CLIMatology
GPCC	Global Precipitation Climatology Centre
GPM	Global Precipitation Measurement
GTS	Global Telecommunication System
KNMI	Royal Netherlands Meteorological Institute
IMERG	Integrated Multi-satellitE Retrievals for GPM
IoT	Internet of Things
LMIC	low- and middle-income country
MNO	mobile network operator
NMHS	national meteorological and hydrological services
OPERA	Operational Program on the Exchange of Weather Radar Information
PWS	personal weather station
QC	quality control
QPE	quantitative precipitation estimation
Radar	RAdio Detection And Ranging
UTC	Universal Time Coordinated
WMO	World Meteorological Organization

References

[1] Becker A, Finger P, Meyer-Christoffer A, *et al*. A description of the global land-surface precipitation data products of the Global Precipitation Climatology Centre with sample applications including centennial (trend) analysis from 1901–present. *Earth Syst Sci Data*. 2013;5:71–99.

[2] Schneider U, Finger P, Rustemeier E, Ziese M, *et al*. Global Precipitation Analysis Products of the GPCC; 2022. Deutscher Wetterdienst, *Abt. Hydrometeorologie, Weltzentrum für Niederschlagsklimatologie (WZN)*. Available from: https://opendata.dwd.de/climate_environment/GPCC/PDF/GPCC_intro_products_lastversion.pdf.

[3] Minda H, and Nakamura K. Coverage of China new generation weather radar network. *Adv Meteorol*. 2019; Article ID 5789358.

[4] Talchabhadel R, Ghimire GR, Sharma S, *et al*. Weather radar in Nepal: Opportunities and challenges in a mountainous region. *Weather*. 2022;77:160–164.

[5] ABI Research. *Wireless Backhaul Evolution Delivering Next-Generation Connectivity*. GSM Association; 2021. Available from: https://www.gsma.com/spectrum/wp-content/uploads/2022/04/wireless-backhaul-spectrum.pdf, accessed 17 May 2023.

[6] Lorenz C, and Kunstmann H. The hydrological cycle in three state-of-the-art reanalyses: Intercomparison and performance analysis. *J Hydrometeorol*. 2012;13:1397–1420.

[7] Kidd CA, Becker A, Huffman GJ, *et al*. So, how much of the Earth's surface is covered by rain gauges? *Bull Am Meteorol Soc*. 2017;98:69–78.

[8] Klein Tank A, *et al*. Daily dataset of 20th-century surface air temperature and precipitation series for the European Climate Assessment. *Int J Climatol*. 2002;22:1441–1453.

[9] Klok EJ, and Klein Tank AMG. Updated and extended European dataset of daily climate observation. *Int J Climatol*. 2008;29:1182–1191.

[10] Van der Schrier G, Overeem A, and Verver G. Improving access to sub-daily rain gauge data; 2021. *EUMETNET, the Copernicus In Situ Coordination Activity*, EEA/DIS/R0/20/001 Lot 1. Available from: https://insitu.copernicus.eu/library/reports/COINS_Report_WP3_raingauges_v2.pdf.

[11] Ericsson. *Ericsson microwave outlook*; 2018. Available from: https://www.ericsson.com/4a312c/assets/local/reports-papers/microwave-outlook/2018/ericsson-microwave-outlook-report-2018.pdf, accessed 10 June 2021.

[12] Uijlenhoet R. Precipitation physics and rainfall observation. In: Bierkens MFP, Dolman AJ, and Troch PA, editors. *Climate and the Hydrological Cycle.* IAHS Special Publication 8. Wallingford: International Association of Hydrological Sciences Press; 2008. p. 59–97.

[13] Barthès L, and Mallet C. Rainfall measurement from the opportunistic use of an Earth–space link in the Ku band. *Atmos Meas Tech*. 2013;6:2181–2193.

[14] Priebe J. *Enabling Climate Services through Mobile Network Operator Data – Opportunities for CML Rainfall Data to Strengthen Rural Climate Resilience*. GSM Association; 2023. Available from: https://www.gsma.com/mobilefordevelopment/wp-content/uploads/2023/02/Enabling-climate-services-through-mobile-network-operator-data.pdf, accessed 21 April 2023.
[15] De Vos LW, Raupach TH, Leijnse H, *et al*. High-resolution simulation study exploring the potential of radars, crowdsourced personal weather stations, and commercial microwave links to monitor small-scale urban rainfall. *Water Resour Res*. 2018;54:10293–10312.
[16] Overeem A. *Commercial Microwave Link Data for Rainfall Monitoring*. Version 2.; 2023. 4TU.ResearchData. Dataset. Available from: https://doi.org/10.4121/7a692e36-c32f-4916-813b-c62d2566e8d8.
[17] Overeem A, Holleman I, and Buishand A. Derivation of a 10-year radar-based climatology of rainfall. *J Appl Meteorol Climatol*. 2009;48:1448–1463.
[18] Overeem A, Leijnse H, and Uijlenhoet R. Measuring urban rainfall using microwave links from commercial cellular communication networks. *Water Resour Res*. 2011;47:W12505.
[19] Joss J, and Waldvogel A. Precipitation measurement and hydrology. In: Battan LJ, and Atlas D, editors. *Radar in Meteorology*. Boston, MA: American Meteorological Society, 1990. p. 577–606.
[20] Fabry F. *Radar Meteorology: Principles and Practice.* Cambridge: Cambridge University Press; 2015.
[21] Rauber RM, and Nesbitt SL. *Radar Meteorology: A First Course*. Hoboken, NJ: John Wiley & Sons; 2018.
[22] Ryzhkov AV, and Zrnic DS. *Radar Polarimetry for Weather Observations*. Cham: Springer Nature Switzerland AG; 2019.
[23] Hazenberg P, Leijnse H, and Uijlenhoet R. Radar rainfall estimation of stratiform winter precipitation in the Belgian Ardennes. *Water Resour Res*. 2011;47:W02507.
[24] Figueras i Ventura J, Boumahmoud AA, Fradon B, *et al*. Long-term monitoring of French polarimetric radar data quality and evaluation of several polarimetric quantitative precipitation estimators in ideal conditions for operational implementation at C-band. *Quart J Roy Meteorol Soc*. 2012; 138(669):2212–2228.
[25] Probert-Jones JR. The radar equation in meteorology. *Quart J Roy Meteorol Soc*. 1962;88:485–495.
[26] Frech M, Hagen M, and Mammen T. Monitoring the absolute calibration of a polarimetric weather radar. *J Atmos Oceanic Technol*. 2017;34(3):599–615.
[27] Saltikoff E, Cho JYN, Tristant P, *et al*. The threat to weather radars by wireless technology. *Bull Amer Meteorol Soc*. 2016;97(7):1159–1167.
[28] Berenguer M, Sempere-Torres D, Corral C, *et al*. A fuzzy logic technique for identifying nonprecipitating echoes in radar scans. *J Atmos Oceanic Technol*. 2006;23(9):1157–1180.
[29] Gourley JJ, Tabary P, and Parent du Chatelet J. A fuzzy logic algorithm for the separation of precipitating from nonprecipitating echoes using

polarimetric radar observations. *J Atmos Oceanic Technol*. 2007;24(8): 1439–1451.

[30] Vulpiani G, Montopoli M, Passeri LD, *et al*. On the use of dual-polarized C-band radar for operational rainfall retrieval in mountainous areas. *J Appl Meteorol Climatol*. 2012;51:405–425.

[31] Crisologo I, Vulpiani G, Abon CC, *et al*. Polarimetric rainfall retrieval from a C-band weather radar in a tropical environment (the Philippines). *Asia-Pac J Atmos Sci*. 2014;50(S):43–55.

[32] Krause JM. A simple algorithm to discriminate between meteorological and nonmeteorological radar echoes. *J Atmos Oceanic Technol*. 2016;33:1875–1885.

[33] Wradlib. wradlib.classify.ClassifyMethods.histo_cut | wradlib; 2023. Retrieved November 2023. Available from: https://docs.wradlib.org/en/latest/generated/wradlib.classify.ClassifyMethods.histo_cut.html.

[34] Gabella M, and Notarpietro R. Ground clutter characterization and elimination in mountainous terrain. In: *Proceedings of the 2nd European Conference on Radar Meteorology ERAD and the COST 717 Mid-Term Seminar*. Katlenburg-Lindau, Copernicus; 2002. p. 305–311. Available from: https://www.copernicus.org/erad/online/erad-305.pdf.

[35] Overeem A, van den Besselaar E, van der Schrier G, *et al*. EURADCLIM: The European climatological high-resolution gauge-adjusted radar precipitation dataset. *Earth Syst Sci Data*. 2023;15:1441–1464.

[36] Saltikoff E, Haase G, Delobbe L, *et al*. OPERA the radar project. *Atmosphere*. 2019;10(6):310.

[37] Michelson DB, and Sunhede D. Spurious weather radar echo identification and removal using multisource temperature information. *Meteorol Appl*. 2004;11:1–14.

[38] Magaldi AV, Bech J, and Lorente J. A multisource scheme based on NWP and MSG data to correct non-precipitating weather radar echoes. *Meteorol Atmos Phys*. 2009;105:121–132.

[39] Hitschfeld W, and Bordan J. Errors inherent in the radar measurement of rainfall at attenuating wavelengths. *J Meteor*. 1954;11(1):58–67.

[40] Germann U. Radome attenuation – A serious limiting factor for quantitative radar measurements? *Meteorol Z*. 1999;8(3):85–90.

[41] Kurri M, and Huuskonen A. Measurements of the transmission loss of a radome at different rain intensities. *J Atmos Oceanic Technol*. 2008;25: 1590–1599.

[42] Tabary P, Vulpiani G, Gourley JJ, *et al*. Unusually high differential attenuation at C Band: Results from a two-year analysis of the French Trappes polarimetric radar data. *J Appl Meteorol Climatol*. 2009;48(10):2037–2053.

[43] Jacobi S, and Heistermann M. Benchmarking attenuation correction procedures for six years of single-polarized C-band weather radar observations in South-West Germany. *Geomat Nat Haz Risk*. 2016;7(6):1785–1799.

[44] Overeem A, de Vries H, Al Sakka H, *et al*. Rainfall-induced attenuation correction for two operational dual-polarization C-band radars in the Netherlands. *J Atmos Oceanic Technol*. 2021;38(6):1125–1142.

[45] Uijlenhoet R, and Berne A. Stochastic simulation experiment to assess radar rainfall retrieval uncertainties associated with attenuation and its correction. *Hydrol Earth Syst Sci*. 2008;12:587–601.
[46] Marzoug M, and Amayenc P. A class of single- and dual-frequency algorithms for rain-rate profiling from a spaceborne radar. Part I: Principle and tests from numerical simulations. *J Atmos Oceanic Technol*. 1994;11: 1480–1506.
[47] Bringi VN, Chandrasekar V, Balakrishnan N, *et al*. An examination of propagation effects in rainfall on radar measurements at microwave frequencies. *J Atmos Oceanic Technol*. 1990;7(6):829–840.
[48] Gorgucci E, Bechini R, Baldini L, *et al.* The influence of antenna radome on weather radar calibration and its real-time assessment. *J Atmos Oceanic Technol*. 2013;30:676–689.
[49] Frasier SJ, Kabeche F, Figueras i Ventura J, *et al*. In-place estimation of wet radome attenuation at X Band. *J Atmos Oceanic Technol*. 2013;30:917–928.
[50] Van de Beek CZ, Leijnse H, Hazenberg P, *et al*. Close-range radar rainfall estimation and error analysis. *Atmos Meas Tech*. 2016;9:3837–3850.
[51] Hazenberg P, Torfs PJJF, Leijnse H, *et al*. Identification and uncertainty estimation of vertical reflectivity profiles using a Lagrangian approach to support quantitative precipitation measurements by weather radar. *J Geophys Res: Atmospheres*. 2013;118:10243–10261.
[52] Marshall JS, Hitschfeld W, and Gunn KLS. Advances in radar weather. In: *Advances in Geophysics*. Vol. 2. Academic Press, New York; 1955. p. 1–56.
[53] Uijlenhoet R. Raindrop size distributions and radar reflectivity–rain rate relationships for radar hydrology. *Hydrol Earth Syst Sci*. 2008;5:615–627.
[54] Vivekanandan J, Zrnic DS, Ellis SM, *et al*. Cloud microphysics retrieval using S-band dual-polarization radar measurements. *Bull Am Meteorol Soc*. 1999;80:381–388.
[55] Park HS, Ryzhkov AV, Zrnić DS, *et al*. The hydrometeor classification algorithm for the polarimetric WSR-88D: Description and application to an MCS. *Weather Forecasting*. 2009;24:730–748.
[56] Bechini R, and Chandrasekar V. A semisupervised robust hydrometeor classification method for dual-polarization radar applications. *J Atmos Oceanic Technol*. 2015;32:22–47.
[57] KNMI. *Precipitation – Gridded Daily Precipitation Sum in the Netherlands*. https://dataplatform.knmi.nl/dataset/rd1-5; 2023. Retrieved May 2023.
[58] KNMI. *Precipitation – 1 Hour Precipitation Accumulations from Climatological Gauge-Adjusted Radar Dataset for The Netherlands (2.4 km) in KNMI HDF5 Format*. https://dataplatform.knmi.nl/dataset/rad-nl21-rac-mfbs-01h-2-0; 2023. Retrieved May 2023.
[59] Holleman I. Bias adjustment and long-term verification of radar-based precipitation estimates. *Meteorol Appl*. 2007;14:195–203.
[60] Goudenhoofdt E, and Delobbe L. Generation and verification of rainfall estimates from 10-yr volumetric weather radar measurements. *J Hydrometeor*. 2016;17(4):1223–1242.

[61] Nelson BR, Prat OP, Seo DJ, *et al*. Assessment and implications of NCEP Stage IV quantitative precipitation estimates for product intercomparisons. *Weather Forecasting*. 2016;31(2):371–394.
[62] Bližňák V, Kašpar M, and Müller M. Radar-based summer precipitation climatology of the Czech Republic. *Int J Climatol*. 2018;38:677–691.
[63] Winterrath T, Brendel C, Hafer M, *et al*. *RADKLIM Version 2017.002: Reprocessed Gauge-Adjusted Radar Data, One-Hour Precipitation Sums (RW)*; 2018.
[64] Park S, Berenguer M, and Sempere-Torres D. Long-term analysis of gauge-adjusted radar rainfall accumulations at European scale. *J Hydrol*. 2019; 573:768–777.
[65] Barton Y, Sideris IV, Raupach TH, *et al*. A multi-year assessment of sub-hourly gridded precipitation for Switzerland based on a blended radar—Rain-gauge dataset. *Int J Climatol*. 2020;40:5208–5222.
[66] Imhoff R, Brauer C, van Heeringen KJ, *et al*. A climatological benchmark for operational radar rainfall bias reduction. *Hydrol Earth Syst Sci*. 2021; 25:4061–4080.
[67] Goudenhoofdt E, and Delobbe L. Evaluation of radar-gauge merging methods for quantitative precipitation estimates. *Hydrol Earth Syst Sci*. 2009;13:195–203.
[68] Saltikoff E, Friedrich K, Soderholm J, *et al*. An overview of using weather radar for climatological studies: Successes, challenges, and potential. *Bull Am Meteorol Soc*. 2019;100(9):1739–1752.
[69] Lengfeld K, Winterrath T, Junghänel T, *et al*. Characteristic spatial extent of hourly and daily precipitation events in Germany derived from 16 years of radar data. *Meteorol Z*. 2019;28(5):363–378.
[70] Fabry F, Meunier V, Treserras BP, *et al*. On the climatological use of radar data mosaics: Possibilities and challenges. *Bull Am Meteorol Soc*. 2017; 98(10):2135–2148.
[71] Bech J, Codina B, Lorente J, *et al*. The sensitivity of single polarization weather radar beam blockage correction to variability in the vertical refractivity gradient. *J Atmos Oceanic Technol*. 2003;20(6):845–855.
[72] Zhang P, Zrnić D, and Ryzhkov A. Partial beam blockage correction using polarimetric radar measurements. *J Atmos Oceanic Technol*. 2013;30(5): 861–872.
[73] Ryzhkov A, Diederich M, Zhang P, *et al*. Potential utilization of specific attenuation for rainfall estimation, mitigation of partial beam blockage, and radar networking. *J Atmos Oceanic Technol*. 2014;31(3):599–619.
[74] Overeem A, Uijlenhoet R, and Leijnse H. Full-year evaluation of non-meteorological echo removal with dual-polarization fuzzy logic for two C-band radars in a temperate climate. *J Atmos Oceanic Technol*. 2020;37(9): 1643–1660.
[75] Kitchen M, and Blackall RM. Representativeness errors in comparisons between radar and gauge measurements of rainfall. *J Hydrol*. 1992;134: 13–33.

[76] Netatmo. Smart Home Weather Station | Netatmo; 2022. Retrieved December 2022. Available from: https://www.netatmo.com/en-eu/smart-weather-station#specifications.
[77] O'Hara T, McClean F, Villalobos Herrera R, *et al*. Filling observational gaps with crowdsourced citizen science rainfall data from the Met Office Weather Observation Website. *Hydrol Res*. 2023;54(4):547–556.
[78] Bell S, Cornford D, and Bastin L. The state of automated amateur weather observations. *Weather*. 2013;68:36–41.
[79] Kirk PJ, Clark MR, Creed E. Weather observations website. *Weather*. 2021; 76:47–49.
[80] Reges HW, Doesken N, Turner J, *et al*. CoCoRaHS: The evolution and accomplishments of a volunteer rain gauge network. *Bull Am Meteorol Soc*. 2016;97(10):1831–1846.
[81] De Vos LW, Leijnse H, Overeem A, *et al*. The potential of urban rainfall monitoring with crowdsourced automatic weather stations in Amsterdam. *Hydrol Earth Syst Sci*. 2017;21:765–777.
[82] Bárdossy A, Seidel J, and El Hachem A. The use of personal weather station observations to improve precipitation estimation and interpolation. *Hydrol Earth Syst Sci*. 2021;25(2):583–601.
[83] Hahn C, Garcia-Marti I, Sugier J, *et al*. Observations from personal weather stations—EUMETNET interests and experience. *Climate*. 2022;10:192.
[84] De Vos LW, Leijnse H, Overeem A, *et al*. Quality control for crowdsourced personal weather stations to enable operational rainfall monitoring. *Geophys Res Lett*. 2019;46:8820–8829.
[85] Ośródka K, Otop I, Szturc J. Automatic quality control of telemetric rain gauge data providing quantitative quality information (RainGaugeQC). *Atmos Meas Technol*. 2022;15(19):5581–5597.
[86] Båserud L, Lussana C, Nipen TN, *et al*. TITAN automatic spatial quality control of meteorological in-situ observations. *Adv Sci Res*. 2020;17: 153–163.
[87] Lussana C, Nipen TN, Båserud L, *et al*. *metno/TITAN: Version 2.1.1 (2.1.1)*. Zenodo; 2020. Available from: https://doi.org/10.5281/zenodo.3667625.
[88] Nipen TN, Oram L, Lussana C, *et al*. *Titanlib Version 0.3.3*; 2022. https://github.com/metno/titanlib.
[89] Overeem A, Leijnse H, van der Schrier G, *et al*. Merging with crowdsourced rain gauge data improves pan-European radar precipitation estimates. *Hydrol Earth Syst Sci Discuss* [preprint]. 2023; https://doi.org/10.5194/hess-2023-122, accepted.
[90] Van de Beek CZ, Leijnse H, Torfs PJJF, *et al*. Seasonal semi-variance of Dutch rainfall at hourly to daily scales. *Adv Water Resour*. 2012;45: 76–85.
[91] De Vos LW. *PWSQC Code*; 2021. https://github.com/LottedeVos/PWSQC.
[92] Van Andel N. *Quality Control Development for Near Real-Time Rain Gauge Networks for Operational Rainfall Monitoring*; 2021. MSc thesis

Utrecht University, Utrecht. Available from: https://studenttheses.uu.nl/handle/20.500.12932/40939.

[93] Overeem A, Leijnse H, and Uijlenhoet R. Retrieval algorithm for rainfall mapping from microwave links in a cellular communication network. *Atmos Meas Technol*. 2016;9:2425–2444.

[94] Overeem A, Leijnse H, De Vos LW, *et al*. *RAINLINK* (v.1.3). Zenodo; 2022. Available from: https://doi.org/10.5281/zenodo.7473635.

[95] KNMI. *Precipitation – 1 Hour Precipitation Accumulations from Climatological Gauge-Adjusted Radar Dataset for The Netherlands (1 km) in KNMI HDF5 Format*. https://dataplatform.knmi.nl/dataset/rad-nl25-rac-mfbs-01h-2-0; 2023. Retrieved April 2023.

[96] KNMI. *Precipitation – 24 Hour Precipitation Accumulations from Climatological Gauge-Adjusted Radar Dataset for The Netherlands (1 km) in KNMI HDF5 Format*. https://dataplatform.knmi.nl/dataset/rad-nl25-rac-mfbs-24h-2-0; 2023. Retrieved April 2023.

[97] Hogg D. Millimeter–wave communication through the atmosphere. *Science*. 1968;159:39–46.

[98] Atlas D, and Ulbrich CW. Path- and area-integrated rainfall measurement by microwave attenuation in the 1-3 cm band. *J Appl Meteor*. 1977;16:1322–1331.

[99] Olsen RL, Rogers DV, and Hodge DB. The aR^b relation in the calculation of rain attenuation. *IEEE Trans Antenn Propag*. 1978;26:318–329.

[100] Leijnse H, Uijlenhoet R, and Stricker JNM. Microwave link rainfall estimation: Effects of link length and frequency, temporal sampling, power resolution, and wet antenna attenuation. *Adv Water Resour*. 2008;31:1481–1493.

[101] Messer H, and Sendik O. A new approach to precipitation monitoring. *IEEE Signal Proc Mag*. 2015;32:110–122.

[102] Uijlenhoet R, Overeem A, and Leijnse H. Opportunistic remote sensing of rainfall using microwave links from cellular communication networks. *WIREs Water*. 2018;5:e1289.

[103] Chwala C, and Kunstmann H. Commercial microwave link networks for rainfall observation: Assessment of the current status and future challenges. *WIREs Water*. 2019;6:e1337.

[104] Upton GJG, Holt AR, Cummings RJ, *et al*. Microwave links: The future for urban rainfall measurement? *Atmos Res*. 2005;77:300–312.

[105] Chwala C, Gmeiner A, Qiu W, *et al*. Precipitation observation using microwave backhaul links in the alpine and pre-alpine region of Southern Germany. *Hydrol Earth Syst Sci*. 2012;16:2647–2661.

[106] Doumounia A, Gosset M, Cazenave F, *et al*. Rainfall monitoring based on microwave links from cellular telecommunication networks: First results from a West African test bed. *Geophys Res Lett*. 2014;41:6016–6022.

[107] Overeem A, Leijnse H, and Uijlenhoet R. Two and a half years of country-wide rainfall maps using radio links from commercial cellular telecommunication networks. *Water Resour Res*. 2016;52:8039–8065.

[108] Polz J, Chwala C, Graf M, *et al*. Rain event detection in commercial microwave link attenuation data using convolutional neural networks. *Atmos Meas Tech*. 2020;13:3835–3853.
[109] Schleiss M, Berne A. Identification of dry and rainy periods using telecommunication microwave links. *IEEE Geosci Remote Sci*. 2010;7:611–615.
[110] Van het Schip TI, Overeem A, Leijnse H, *et al*. Rainfall measurement using cell phone links: Classification of wet and dry periods using geostationary satellites. *Hydrolog Sci J*. 2017;62:1343–1353.
[111] Kharadly MMZ, and Ross R. Effect of wet antenna attenuation on propagation data statistics. *IEEE Trans Antenn Propag*. 2001;49:1183–1191.
[112] Leijnse H, Uijlenhoet R, and Stricker JNM. Rainfall measurement using radio links from cellular communication networks. *Water Resour Res*. 2007; 43:n/a–n/a. W03201.
[113] Leijnse H, Uijlenhoet R, and Stricker JNM. Hydrometeorological application of a microwave link: 2. Precipitation. *Water Resour Res*. 2007;43:n/a–n/a. W04417.
[114] Schleiss M, Rieckermann J, and Berne A. Quantification and modeling of wet-antenna attenuation for commercial microwave links. *IEEE Geosci Remote Sci*. 2013;10:1195–1199.
[115] Pastorek J, Fencl M, Rieckermann J, *et al*. Precipitation estimates from commercial microwave links: Practical approaches to wet-antenna correction. *IEEE Trans Geosci Remote Sens*. 2022;60:Art no. 4104409.
[116] Rios Gaona MF, Overeem A, Leijnse H, *et al*. Measurement and interpolation uncertainties in rainfall maps from cellular communication networks. *Hydrol Earth Syst Sci*. 2015;19:3571–3584.
[117] Graf M, Chwala C, Polz J, *et al*. Rainfall estimation from a German-wide commercial microwave link network: Optimized processing and validation for 1 year of data. *Hydrol Earth Syst Sci*. 2020;24:2931–2950.
[118] Fencl M, Rieckermann J, Sýkora P, *et al*. Commercial microwave links instead of rain gauges: Fiction or reality? *Water Sci Technol*. 2015;71:31–37.
[119] Messer HA, Zinevich A, Alpert P. Environmental monitoring by wireless communication networks. *Science*. 2006;312:713.
[120] Rayitsfeld A, Samuels R, Zinevich A, *et al*. Comparison of two methodologies for long term rainfall monitoring using a commercial microwave communication system. *Atmos Res*. 2012;104–105:119–127.
[121] Overeem A, Leijnse H, and Uijlenhoet R. Country-wide rainfall maps from cellular communication networks. *Proc Natl Acad Sci USA*. 2013;110: 2741–2745.
[122] De Vos LW, Overeem A, Leijnse H, *et al*. Rainfall estimation accuracy of a nationwide instantaneously sampling commercial microwave link network: Error dependency on known characteristics. *J Atmos Ocean Technol*. 2019; 36:1267–1283.
[123] Chwala C, Keis F, and Kunstmann H. Real-time data acquisition of commercial microwave link networks for hydrometeorological applications. *Atmos Meas Technol*. 2016;9:991–999.

[124] Djibo M, Ouedraogo WYSB, Doumounia A, *et al*. Towards innovative solutions for monitoring precipitation in poorly instrumented regions: Real-time system for collecting power levels of microwave links of mobile phone operators for rainfall quantification in Burkina Faso. *Appl Syst Innov*. 2023; 6(4).

[125] RAINLINK. *GitHub – Overeem11/RAINLINK: Retrieval Algorithm for Rainfall Mapping from Microwave Links in a Cellular Communication Network*; 2022. Available from: https://github.com/overeem11/RAINLINK, accessed 23 November 2023.

[126] Mercier F, Barthès L, and Mallet C. Estimation of finescale rainfall fields using broadcast TV satellite links and a 4DVAR assimilation method. *J Atmos Ocean Technol*. 2015;32:1709–1728.

[127] Graf M, El Hachem A, Eisele M, *et al*. Rainfall estimates from opportunistic sensors in Germany across spatio-temporal scales. *J Hydrol: Regional Stud*. 2021;37:1448–1463.

[128] Barnes SL. A technique for maximizing details in numerical weather map analysis. *J Appl Meteorol*. 1964;3:396–409.

[129] Overeem A, Leijnse H, and Uijlenhoet R. Quantitative precipitation estimation using commercial microwave links. In: Moore RJ, Cole SJ, and Illingworth AJ, editors. *Weather Radar and Hydrology, Proceedings of a Symposium Held in Exeter, UK*, April 2011. IAHS Publ. 351, IAHS Press, Wallingford, Oxfordshire; 2012. p. 129–134.

[130] Wenzel M, Vogel C, Graf M, *et al*. Development of a Python Framework (pyRadman) for QPE using radar and CML data at DWD. In: *EGU General Assembly 2023*, Vienna, Austria, 24–28 Apr 2023; 2023. p. EGU23–13779.

[131] Haese B, Hörning S, Chwala C, *et al*. Stochastic reconstruction and interpolation of precipitation fields using combined information of commercial microwave links and rain gauges. *Water Resour Res*. 2017;53:10740–10756.

[132] Blettner N, Chwala C, Haese B, *et al*. Combining commercial microwave link and rain gauge observations to estimate countrywide precipitation: A stochastic reconstruction and pattern analysis approach. *Water Resour Res*. 2022;58:e2022WR03256.

[133] Paulson K, and Al-Mreri A. A rain height model to predict fading due to wet snow on terrestrial links. *Radio Sci*. 2011;46:n/a–n/a. RS4010.

[134] Imhoff RO, De Cruz L, Dewettinck W, *et al*. Scale-dependent blending of ensemble rainfall nowcasts and numerical weather prediction in the open-source pysteps library. *Quart J Roy Meteorol Soc*. 2023;149:1335–1364.

[135] Hoedjes JCB, Kooiman A, Maathuis BHP, *et al*. A conceptual flash flood early warning system for Africa, based on terrestrial microwave links and flash flood guidance. *ISPRS Int J Geo-Inf*. 2014;3:584–598.

[136] Rios Gaona MF, Overeem A, Raupach TH, *et al*. Rainfall retrieval with commercial microwave links in São Paulo, Brazil. *Atmos Meas Technol*. 2018;11:4465–4476.

[137] Sohail Afzal M, Shah SHH, Cheema MJM, *et al*. Real time rainfall estimation using microwave signals of cellular communication networks: A case study of Faisalabad, Pakistan. *Hydrol Earth Syst Sci Discuss*. 2018.

[138] GSM Association. *Mobile Technology for Rural Climate Resilience: The Role of Mobile Operators in Bridging the Data Gap*; 2019. Available from: https://www.gsma.com/mobilefordevelopment/wp-content/uploads/2019/10/GSMA_AgriTech_Climate_Report.pdf, accessed 10 June 2021.

[139] Overeem A, Leijnse H, van Leth TC, *et al*. Tropical rainfall monitoring with commercial microwave links in Sri Lanka. *Environ Res Lett*. 2021;16:074058.

[140] Rios Gaona MF, Overeem A, Brasjen AM, *et al*. Evaluation of rainfall products derived from satellites and microwave links for the Netherlands. *IEEE Trans Geosci Remote Sens*. 2017;55:6849–6859.

[141] Imhoff RO, Overeem A, Brauer CC, Leijnse H, Weerts AH, and Uijlenhoet R. Rainfall nowcasting using commercial microwave links. *Geophys Res Lett*. 2020;47:e2020GL089365.

[142] Brauer CC, Overeem A, Leijnse H, *et al*. The effect of differences between rainfall measurement techniques on groundwater and discharge simulations in a lowland catchment. *Hydrol Process*. 2016;30:3885–3900.

[143] Smiatek G, Keis F, Chwala C, *et al*. Potential of commercial microwave link network derived rainfall for river runoff simulations. *Environ Res Lett*. 2017;12:034026.

[144] Pastorek J, Fencl M, Rieckermann J, *et al*. Commercial microwave links for urban drainage modelling: The effect of link characteristics and their position on runoff simulations. *J Environ Manage*. 2019;251:109522.

[145] Met Office. *Cartopy: A Cartographic Python Library with a Matplotlib Interface*. Exeter, Devon; 2022. Available from: https://scitools.org.uk/cartopy/docs/latest/.